

A segmentation-free isogeometric extended mortar contact method

Thang X. Duong¹, Laura De Lorenzis², Roger A. Sauer¹

¹ *Aachen Institute for Advanced Study in Computational Engineering Science (AICES),
RWTH Aachen University, Germany*

² *Institute of Applied Mechanics, Technische Universität Braunschweig, Germany*

Abstract: This paper presents a new isogeometric mortar contact formulation based on an extended finite element interpolation to capture physical pressure discontinuities at the contact boundary. The so called two-half-pass algorithm is employed, which leads to an unbiased formulation and, when applied to the mortar setting, has the additional advantage that the mortar coupling term is no longer present in the contact forces. As a result, the computationally expensive segmentation at overlapping master-slave element boundaries, usually required in mortar methods (although often simplified with loss of accuracy), is not needed from the outset. For the numerical integration of general contact problems, the so-called *refined boundary quadrature* is employed, which is based on adaptive partitioning of contact elements along the contact boundary. The contact patch test is examined and compared for various contact formulations. It turns out that the classical penalty mortar formulation does not pass the patch test, whereas the proposed formulation passes the test without segmentation and refined boundary quadrature. Several numerical examples are presented to demonstrate the robustness and accuracy of the proposed formulation.

Keywords: computational contact mechanics, isogeometric analysis, mortar methods, segmentation, extended finite element methods.

1 Introduction

This paper aims at developing a new mortar method that is unbiased and is able to capture physical discontinuities of the contact pressure at contact boundaries. We are concerned with nonlinear contact involving arbitrarily large deformation and sliding in the context of isogeometric analysis (IGA) (Hughes et al., 2005).

In mortar methods, the contact constraints are enforced in a weak sense. This approach originates from domain decomposition, which provides a rigorous mathematical background for proving stability and optimal convergence rates, see e.g. Puso and Laursen (2004a); Hartmann and Ramm (2008); Hesch and Betsch (2008); Temizer (2012); De Lorenzis et al. (2014) and references therein.

Existing mortar formulations differ mainly on the choice of shape functions for the approximation of the contact pressure. We will refer to these shape functions as *mortar shape functions* (Duong et al., 2017b). For instance, in the formulation of Puso and Laursen (2004a), the mortar shape functions are identical to the standard shape functions of the displacement field, De Lorenzis et al. (2012) employ weighted standard shape functions, and Popp et al. (2012) use dual shape functions that are constructed from a local biorthogonality condition. As shown in

¹corresponding author, email: sauer@aices.rwth-aachen.de

Duong et al. (2017b), all above choices can be derived systematically from least-squares conditions. Note that all existing mortar formulations are biased, i.e. the computational results depend on the choice of slave and master surface.

The application of IGA to contact problems has been shown to be highly advantageous in terms of robustness (De Lorenzis et al., 2014). This is due to the fact that the IGA discretizations (i.e. NURBS, T-Splines) can provide smoothness of any order across element boundaries. This feature is generally beneficial for contact computations with large displacements and large sliding. A number of works have studied mortar methods in the context of IGA (e.g. Temizer et al. (2011); De Lorenzis et al. (2012); Kim and Youn (2012); Dittmann et al. (2014); Brivadis et al. (2015); Seitz et al. (2016)).

However, within the discretized system, there may exist various discontinuities of the contact pressure that can reduce either the accuracy or the robustness of the simulation. Here, we classify discontinuities into two categories: *physical* and *artificial* discontinuities. The first one is independent of the contact formulation and discretization, and they should be recovered as accurately as possible in contact computations. In contrast, *artificial* discontinuities may appear due to discretization methods or due to the underlying theory used to describe the contact problem. *Artificial* discontinuities are further classified into *geometric* and *theoretical* discontinuities. *Geometric* discontinuities are caused by discontinuities of normal vectors, while *theoretical* discontinuities appear due to discontinuities of shape functions and their products. An example of theoretical discontinuities are the discontinuities of the mortar coupling term at the overlapping boundaries of slave and master elements in standard mortar formulations. These discontinuities appear even for high order NURBS discretizations (Seitz et al., 2016).

Geometric and *theoretical* discontinuities do not necessarily exclude each other. For instance, at the interface between two NURBS patches, since both normal vectors and shape functions can be discontinuous, the *geometric* and *theoretical* discontinuities of the contact pressure coincide. However, *physical* and *artificial* discontinuities are exclusive. But they may be captured and caused by the same quantities (such as normal vectors, shape functions, and their products).

We note that a discontinuity of the normal vector field usually leads to a (strong, physical and/or artificial) discontinuity of the contact pressure, but the presence of the latter is not necessarily accompanied by the former. For instance, the contact of two balls results in a (weak) physical discontinuity of the contact pressure, while the geometry is still smooth.

On one hand, *artificial* discontinuities usually lead to discretization and quadrature errors on discretized contact surfaces. In classical mortar methods, the segmentation approach can treat *artificial* discontinuities at the overlapping boundaries of slave and master elements, see e.g. Puso and Laursen (2004a); Hesch and Betsch (2011); Popp et al. (2013); Wilking and Bischoff (2017). However, segmentation is usually expensive in terms of computation time, while it is still needed even for IGA discretizations (Brivadis et al., 2015; Seitz et al., 2016).

On the other hand, *physical* discontinuities may lead to interpolation and/or quadrature errors within element (i.e. local) domains. In the classical Gauss-point-to-segment (GPTS) contact formulation with penalty contact, *physical* discontinuities are captured by constitutive laws and thus no interpolation error appears. However, the accuracy may still reduce drastically at the contact boundaries, since *physical* discontinuities may not be resolved properly by standard quadrature. In order to tackle this problem, Duong and Sauer (2015) have proposed a so-called *refined boundary quadrature* (RBQ) technique, which is based on adaptive partitioning of the surface finite elements that contain the contact boundary.

For mortar methods, *physical* discontinuities can be captured by so-called consistent dual shape function (Cichosz and Bischoff, 2011; Popp et al., 2012; Seitz et al., 2016). However, since the consistency treatment is originally motivated by ensuring the biorthogonality condition for the

dual shape function on elements that are partially in contact, to the best of our knowledge, only *strong* physical discontinuities are considered by the approach.

In our mind, the need for consistency not only concerns the loss of biorthogonality that follows from a particular choice of the mortar shape function. More importantly, consistency also concerns the recovery of the physical discontinuities of the contact pressure at the contact boundary. In fact, in order to pass the patch test, recovering the strong physical discontinuity is indispensable. For this reason, it should be noted that increasing the number of quadrature points does not solve the problem. Therefore, the consistency for *weak* physical discontinuities may be required as well. Examination from examples 8.1 and 8.2 in this paper shows that the error in contact forces is quite significant for coarse meshes.

In principle, the consistency of dual shape functions for weak physical discontinuities can also be obtained by the same approach as for strong physical discontinuities. Note, however, that a major deficiency of consistent dual shape functions is ill-conditioning of the stiffness matrix when the contact boundary approaches any element boundaries (Cichosz and Bischoff, 2011; Popp et al., 2013). This is due to the fact that dual shape functions are constructed from inverting mass matrices that are approaching zero (Duong et al., 2017b).

Further, it should be noted that both discretization and interpolation errors due to the above-mentioned discontinuities can be reduced by mesh refinement. This approach, however, diminishes an important advantage of NURBS discretizations, i.e. that the geometry can be represented accurately with coarse meshes.

In this contribution, we thus propose an extended finite element (XFEM) interpolation to recover the physical discontinuities of the contact pressure. The new formulation is accordingly denoted the *extended mortar method*. The central issue of this approach is the explicit detection of the contact boundaries. Here, we will use the level-set method proposed by Duong and Sauer (2015). The level-set function is then used as the enrichment function to recover the physical discontinuities. Therefore, both weak and strong physical discontinuities are accounted for in the contact formulation. In order to reduce the quadrature error associated with recovering physical discontinuities, we employ the RBQ technique as done for GPTS in Duong and Sauer (2015).

Besides, the artificial discontinuities are also treated. In order to eliminate the mortar coupling term that causes the theoretical discontinuities, we apply the so-called *two-half-pass* approach (Sauer and De Lorenzis, 2013, 2015). In this approach, the two bodies in contact are treated equally, i.e. there is no distinction between slave and master surfaces. This is done by considering two passes with alternating slave and master roles, but only accounting for the forces acting on the slave surface. This leads to an unbiased contact formulation that does not contain the mortar coupling term - responsible for the expensive segmentation - in the contact force vectors. Segmentation can thus be avoided without any loss of accuracy.

The remaining part of this paper is organized as follows: Sec. 2 presents the contact kinematics. Sec. 3 defines various contact pressures and discusses work-conjugated contact variables. In Sec. 4 The existing mortar formulations are summarized. For comparison, we also present its two-half-pass version. Discontinuities and quadrature schemes are also discussed. Sec. 5 presents the extended mortar contact in full-pass and two-half-pass version. Sec. 6 unifies contact formulations for GPTS, existing mortar methods, and the proposed extended mortar method. Sec. 7 examines the patch test for various contact formulations. Several numerical examples are presented in Sec. 8. Finally, Sec. 9 concludes the paper.

2 Contact kinematics

This section presents different measures for the normal contact gap and its variation. In order to account for non-smoothness due to discretization, kinematical variables are defined directly for the discretized system.

Consider two discretized surfaces in the current configuration that are coming into contact: slave surface Γ^s and master surface Γ^m . The two surfaces consist in total of n_{el} elements, numbered $e = 1, \dots, n_{el}$. Each element e contains n_e nodes (or control points), and occupies the domain Γ^e in the current configuration. Any point $\mathbf{x} \in \Gamma^e$ is associated with a coordinate $\boldsymbol{\xi}$ in the parameter domain \mathcal{P} , and can be interpolated from the nodal positions, \mathbf{x}_A , by the standard shape functions N_A as

$$\mathbf{x}(\boldsymbol{\xi}) = \sum_{A=1}^{n_e} N_A(\boldsymbol{\xi}) \mathbf{x}_A = \mathbf{N}_e \mathbf{x}_e, \quad \boldsymbol{\xi} \in \mathcal{P}, \quad (1)$$

where $\mathbf{N}_e := [N_1 \mathbf{I}, N_2 \mathbf{I}, \dots, N_{n_e} \mathbf{I}]$ and $\mathbf{x}_e := [\mathbf{x}_1, \mathbf{x}_2, \dots, \mathbf{x}_{n_e}]^T$ denote the element shape function and elemental node arrays, respectively.

On the contact surfaces, a set of tangent vectors can be defined by

$$\mathbf{a}_\alpha := \frac{\partial \mathbf{x}}{\partial \xi^\alpha} = \mathbf{N}_{e,\alpha} \mathbf{x}_e, \quad (\alpha = 1, 2), \quad (2)$$

where $\mathbf{N}_{e,\alpha} := \partial \mathbf{N}_e / \partial \xi^\alpha$. The normal vector at $\boldsymbol{\xi}$ is given by

$$\mathbf{n} := \frac{\mathbf{a}_1 \times \mathbf{a}_2}{\|\mathbf{a}_1 \times \mathbf{a}_2\|}. \quad (3)$$

With Eqs. (2) and (3), we can define the components of the metric tensor,

$$a_{\alpha\beta} = \mathbf{a}_\alpha \cdot \mathbf{a}_\beta, \quad (4)$$

and those of the curvature tensor,

$$b_{\alpha\beta} = \mathbf{n} \cdot \mathbf{a}_{\alpha,\beta} = \mathbf{n} \cdot \mathbf{N}_{e,\alpha\beta} \mathbf{x}_e. \quad (5)$$

Similarly, in the reference configuration, tangent vectors \mathbf{A}_α and metric tensor components $A_{\alpha\beta}$ can be defined. From the metric tensors, the surface stretch of the contact surfaces is given by

$$J := \frac{\sqrt{\det[a_{\alpha\beta}]}}{\sqrt{\det[A_{\alpha\beta}]}} = \frac{\|\mathbf{a}_1 \times \mathbf{a}_2\|}{\|\mathbf{A}_1 \times \mathbf{A}_2\|}. \quad (6)$$

2.1 Raw gap

Let \mathcal{E}_s and \mathcal{E}_m be the sets of the element numbers in the slave and master surfaces, respectively. The pointwise normal *raw gap* g_n at position $\mathbf{x} \in \Gamma^e$, with $e \in \mathcal{E}_s$, is defined as

$$g_n(\boldsymbol{\xi}) := \mathbf{n}_p \cdot (\mathbf{x}(\boldsymbol{\xi}) - \mathbf{x}_p), \quad \boldsymbol{\xi} \in \mathcal{P}, \quad (7)$$

where $\mathbf{x}_p := \mathbf{x}(\boldsymbol{\xi}_p) \in \Gamma^{\hat{e}}$, with $\hat{e} \in \mathcal{E}_m$, denotes the closest projection point of \mathbf{x} onto the master surface with $\boldsymbol{\xi}_p$ being the corresponding coordinate in \mathcal{P} ; \mathbf{n}_p denotes the normal vector defined by $\mathbf{n}_p := \mathbf{n}(\boldsymbol{\xi}_p)$. The variation of g_n follows from Eq. (7) and (1) as (Wriggers, 2006)

$$\delta g_n = \mathbf{n}_p \cdot (\mathbf{N}_e \delta \mathbf{x}_e - \mathbf{N}_p \delta \mathbf{x}_{\hat{e}}), \quad (8)$$

where $\mathbf{N}_p := \mathbf{N}_{\hat{e}}(\boldsymbol{\xi}_p)$.

2.2 Weighted nodal gap

The *weighted nodal gap* is defined by

$$\tilde{g}_{nA} := \int_{\Gamma_0^A} M_A g_n \, dA_s, \quad (9)$$

where $\Gamma_0^A \subseteq \Gamma_0^s$ is the support area of node A in the reference configuration, and M_A is called *mortar shape function*. Eq. (9) realizes the (mortar) projection of the raw gap (7) onto the nodal degrees of freedom. Several choices of M_A are listed in Tab. 1 based on the least squares approach by Duong et al. (2017b).

Mortar types	Mortar shape functions	Mass matrices
M-GLS (Global least-squares)	$M_A := \sum_B N_B [L_{BA}]^{-1}$	$L_{AB} := \int_{\Gamma_0^s} N_A N_B \, dA_s$
M-GLS* (Global least-squares, PU)	$M_A := \sum_{B,C} N_B [L_{BC}]^{-1} W_{CA}$	
M-LmLS (Lumped least-squares; or weighted std. shape fnc.)	$M_A := \sum_B N_B W_{BA}^{-1}$	$W_{CA} := \delta_{CA} \int_{\Gamma_0^s} N_A \, dA_s$
M-LmLS* (Lumped least-squares, PU; or standard shape function)	$M_A := N_A$	
M-LcLS (Local least-squares)	$M_A := \sum_{B,C,D} N_B [L_{BC}^e]^{-1} W_{CD}^e W_{DA}^{-1}$	$L_{AB}^e := \int_{\Gamma_0^e \subseteq \Gamma_0^s} N_A N_B \, dA_s$
M-LcLS* (Local least-squares, PU; or dual shape functions)	$M_A := \sum_{B,C} N_B [L_{BC}^e]^{-1} W_{CA}^e$	$W_{CA}^e := \delta_{CA} \int_{\Gamma_0^e \subseteq \Gamma_0^s} N_A \, dA_s$

Table 1: Summary of mortar shape functions M_A based on various least-squares approaches (Duong et al., 2017b): (*) indicates satisfaction of the partition of unity (PU). Note that M-LmLS, M-LmLS*, and M-LcLS* are equivalent to the shape functions used in existing formulations, i.e. of De Lorenzis et al. (2012), Puso and Laursen (2004a), and Popp et al. (2012), respectively.

Note that the integration domain here is the fixed reference configuration. This choice will significantly simplify the variation and linearization. Nevertheless, it would also be possible to define operator (9) in the current configuration, or on an intermediate surface.

Considering that M_A is independent from the deformation, the variation of \tilde{g}_{nA} according to Eq. (9) reads

$$\delta \tilde{g}_{nA} = \int_{\Gamma_0^A} M_A \delta g_n \, dA_s. \quad (10)$$

2.3 Smoothed versus mortar gap

The so-called (pointwise) *smoothed gap*, \hat{g}_n , is defined by

$$\hat{g}_n(\boldsymbol{\xi}) := \sum_{A=1}^{n_e} N_A(\boldsymbol{\xi}) \tilde{g}_{nA} = \bar{\mathbf{N}}_e \bar{\mathbf{g}}_n^e, \quad (11)$$

where $\bar{\mathbf{N}}_e := [N_1, N_2, \dots, N_{n_e}]$ and $\tilde{\mathbf{g}}_n^e := [\tilde{g}_{n1}, \tilde{g}_{n2}, \dots, \tilde{g}_{nn_e}]^T$ denote the elemental shape function array and the elemental weighted nodal gap array, respectively.

Similarly, the so-called (pointwise) *mortar gap*, g_n^* , is defined by

$$g_n^*(\boldsymbol{\xi}) := \sum_{A=1}^{n_e} M_A(\boldsymbol{\xi}) \tilde{g}_{nA} = \mathbf{M}_e \tilde{\mathbf{g}}_n^e, \quad (12)$$

where $\mathbf{M}_e := [M_1, M_2, \dots, M_{n_e}]$, and where we have assumed that M_A has the same support area as N_A .² Thus, the corresponding variations of \hat{g}_n and g_n^* read

$$\delta \hat{g}_n = \sum_{A=1}^{n_e} N_A \delta \tilde{g}_{nA} = \bar{\mathbf{N}}_e \delta \tilde{\mathbf{g}}_n^e, \quad (13)$$

$$\delta g_n^* = \sum_{A=1}^{n_e} M_A \delta \tilde{g}_{nA} = \mathbf{M}_e \delta \tilde{\mathbf{g}}_n^e. \quad (14)$$

3 Contact pressures and work conjugate contact pairs

In Sec. 2, we have presented various contact gap measures. In this section we define the corresponding contact pressures and discuss work conjugate contact pairs in the context of mortar methods.

3.1 Raw pressure

For the penalty method, the pointwise *raw contact pressure* at $\boldsymbol{\xi} \in \mathcal{P}$ is defined by

$$p(\boldsymbol{\xi}) := \epsilon_n g_n, \quad (15)$$

where the constant ϵ_n is a deformation-independent penalty parameter. Thus, p is the nominal pressure, representing the contact force per reference area. It is related to the true contact pressure (Puso and Laursen, 2004a; Popp et al., 2012; Seitz et al., 2016) by

$$p^{\text{true}} = J^{-1} p = J^{-1} \epsilon_n g_n =: \bar{\epsilon}_n g_n. \quad (16)$$

Here, J is the surface stretch defined by Eq. (6), and $\bar{\epsilon}_n$ is now a deformation-dependent penalty parameter.

3.2 Weighted nodal pressure

For the penalty method, the weighted nodal pressure, denoted \tilde{p}_A , can be defined by (see e.g. Temizer et al. (2011))

$$\tilde{p}_A := \epsilon_n \chi_A \tilde{g}_{nA} = \chi_A \int_{\Gamma_0^A} M_A \epsilon_n g_n \, dA_s, \quad (17)$$

where $\chi_A := \frac{1}{2} [1 - \text{sign}(\tilde{g}_{nA})]$ is an active variable at node A that ensures that $\tilde{p}_A = 0$ for $\tilde{g}_{nA} > 0$.

²For the general case, n_e would simply be extended to contain all nodes whose support areas cover $\boldsymbol{x}(\boldsymbol{\xi})$

3.3 Smoothed and mortar contact pressure

Analogous to Eqs. (11) and (12), the so-called *smoothed contact pressure* \hat{p} , and the *mortar contact pressure* p^* can be defined by

$$\hat{p}(\boldsymbol{\xi}) := \sum_{A=1}^{n_e} N_A(\boldsymbol{\xi}) \tilde{p}_A = \bar{\mathbf{N}}_e \tilde{\mathbf{p}}^e, \quad (18)$$

and

$$p^*(\boldsymbol{\xi}) := \sum_{A=1}^{n_e} M_A(\boldsymbol{\xi}) \tilde{p}_A = \mathbf{M}_e \tilde{\mathbf{p}}^e, \quad (19)$$

respectively, where $\tilde{\mathbf{p}}^e := [\tilde{p}_1, \tilde{p}_2, \dots, \tilde{p}_{n_e}]^T$ denotes the elemental weighted nodal pressure array.

3.4 Contact work conjugation

Each pair of gap and pressure measures results in a different contact formulation. Tab. 2 lists the work-conjugate pairs that are used in classical Node-to-segment (NTS), GPTS, and mortar contact formulations.

contact formulation	work-conjugate pairs	3. KT cond.	contact pressure
GPTS	(p, g_n)	$p g_n = 0$	$p = p(g_n)$
NTS	$(p_A := p(\boldsymbol{\xi}_A), g_{nA} := g_n(\boldsymbol{\xi}_A))$	$p_A g_{nA} = 0$	$p_A = p_A(g_{nA})$
Generalized mortar: (a) penalty method (b) Lagrange multiplier	(\hat{p}, \hat{g}_n)	$\hat{p} \hat{g}_n = 0$	$\hat{p} = \sum_{A=1}^{n_e} N_A \tilde{p}_A$ (a) $\tilde{p}_A = \tilde{p}_A(\tilde{g}_{nA})$ (b) $\tilde{p}_A = \text{unknown}$
Standard mortar: (a) penalty method (b) Lagrange multiplier	equivalent pairs: $(\tilde{p}_A, \tilde{g}_{nA})$ or (p^*, g_n) or (p, g_n^*)	$\tilde{p}_A \tilde{g}_{nA} = 0$; or $p^* g_n = 0$; or $p g_n^* = 0$.	$p^* = \sum_{A=1}^{n_e} M_A \tilde{p}_A$ (a) $\tilde{p}_A = \tilde{p}_A(\tilde{g}_{nA})$ (b) $\tilde{p}_A = \text{unknown}$

Table 2: Contact work-conjugate pairs and corresponding contact formulations: The Kuhn-Tucker (KT) conditions for the node-to-segment (NTS) can be obtained by requiring the KT conditions from the GPTS formulation to be satisfied discretely at nodes/knots. Likewise, the standard mortar formulation is a special case of the generalized mortar formulation.

In particular, for the standard mortar formulation (e.g. by [Puso and Laursen \(2004a\)](#); [De Lorenzis et al. \(2012\)](#)), the third Kuhn-Tucker condition is enforced in a weak sense by the discrete equation $\tilde{p}_A \tilde{g}_{nA} = 0$, for each $A = 1, \dots, n_s$, where n_s denotes the number of slave nodes. These equations can also be obtained by requiring the Kuhn-Tucker condition from the so-called generalized mortar formulation to be satisfied only at nodes or knots (see Tab. 2). Besides, by means of Eqs. (9) and (17), their contact potential can be shown to satisfy

$$\Pi_c = \sum_{A=1}^{n_s} \tilde{p}_A \tilde{g}_{nA} = \int_{\Gamma_0^s} p^* g_n dA_s = \int_{\Gamma_0^s} p g_n^* dA_s. \quad (20)$$

Thus, (p^*, g_n) and (p, g_n^*) are equivalent work-conjugate pairs to $(\tilde{p}_A, \tilde{g}_{nA})$. In view of (20), the mortar pressure p^* is always the (approximated) nominal pressure for any mortar shape function M_A . Furthermore, in view of Eqs. (9) and (17), the mortar method can be interpreted as a smoothing of the raw contact gap g_n . In principle, the concept of the smoothing can be extended further by considering \hat{g}_n as the raw contact gap and performing the smoothing process once again. Similarly, new mortar formulations can be derived by combining different work-conjugate pairs.

4 Standard mortar contact

In this section, we first summary the finite element contact forces for the three standard mortar formulations of Eq. (20). Since these formulations employ a full-pass algorithm, we denote them *standard mortar full-pass (SMFP)* formulations. Next, since these formulations are biased w.r.t. the choice of slave and master surfaces, we will modify them by the so-called two-half-pass approach (Sauer and De Lorenzis, 2013, 2015). The modified formulation is thus called *standard mortar two-half-pass (SM2HP)* formulation. Further, discontinuities in the considered contact formulations are also discussed. It will also be shown that the SM2HP formulation can avoid the segmentation as is required in SMFP.

4.1 Standard mortar full-pass contact (SMFP)

4.1.1 Finite element contact forces

The contact virtual work for SMFP can be obtained by taking the variation of contact potential (20) w.r.t. the displacement. That is,

$$\delta\Pi_c = \sum_{e \in \mathcal{E}_s} \int_{\Gamma_0^e} p^* \delta g_n \, dA_e . \quad (21)$$

By taking Eq. (8) into account, we obtain

$$\delta\Pi_c = \sum_{e \in \mathcal{E}_s} (\delta \mathbf{x}_e \cdot \mathbf{f}_e + \delta \mathbf{x}_{\hat{e}} \cdot \mathbf{f}_{\hat{e}}) , \quad (22)$$

where $\hat{e} \in \mathcal{E}_m$ denotes the master element(s) that contain closest projection points emanating from the slave element e , and where

$$\mathbf{f}_e := \int_{\Gamma_0^e} \mathbf{N}_e^T \mathbf{T}_c^* \, dA_e \quad \text{and} \quad \mathbf{f}_{\hat{e}} := - \int_{\Gamma_0^e} \mathbf{N}_p^T \mathbf{T}_c^* \, dA_e \quad (23)$$

are the finite element contact forces with the nominal contact traction defined by

$$\mathbf{T}_c^* := p^* \mathbf{n}_p . \quad (24)$$

4.1.2 Discontinuities

Global contact equilibrium requires $\delta\Pi_c = 0$ and follows from Eq. (22) as

$$\sum_{A=1}^{n_s} \int_{\Gamma_0^s} N_A p^* \mathbf{n}_p \, dA_s = \sum_{B=1}^{n_m} \int_{\Gamma_0^s} N_B(\boldsymbol{\xi}_p) p^* \mathbf{n}_p \, dA_s , \quad (25)$$

where n_m denotes the number of master nodes. Eq. (25) is satisfied when the integration on both sides is exact. However, there may exist discontinuities in the integrands: *physical discontinuities* of p^* and/or \mathbf{n}_p at the contact boundaries, *geometric discontinuities* of \mathbf{n}_p , and/or *theoretical discontinuities* of $N_B(\boldsymbol{\xi}_p) \cdot M_A(\boldsymbol{\xi})$. Therefore, two aspects must be considered here: (1) accurately capturing the physical discontinuities and (2) accurate quadrature. In classical approaches, the so-called consistent mortar shape function can be used to capture the (strong) physical discontinuity (Popp et al., 2012; Seitz et al., 2016), while segmentation is used for quadrature (see e.g. Puso and Laursen (2004a)). Quadrature is discussed in the following.

4.1.3 Numerical quadrature

Numerical quadrature is used for the evaluation of the contact forces (23). Since discontinuities may appear in integrands, a suitable quadrature scheme should be chosen for accurate integration. The simplest method is using a large number of quadrature points (see De Lorenzis et al. (2012)). Such a scheme, however, is not robust and accurate since strong discontinuities cannot be captured well by this method.

Alternatively, a more robust and accurate approach is segmentation, which requires to split (or segment) the integration domain at interfaces where the integrands are discontinuous e.g. at the overlapping boundaries of master-slave elements (Puso and Laursen, 2004a). Note that at the overlapping boundaries for Lagrange elements, both geometric and theoretical discontinuities coincide.

Moreover, for NURBS, since the artificial (theoretical) discontinuities are present at overlapping boundaries of master-slave elements, in principle, the segmentation is required there as well. The requirement is especially important at the patch boundaries if multiple patches are used, since additional geometric discontinuities appear in this case.

Segmentation, however, reduces the efficiency of the contact formulation significantly. In this paper, we thus also aim at developing a contact formulation that avoids costly segmentation. With this in mind, we consider the so-called *two-half-pass* approach, which is extended to mortar contact in the following section.

4.2 Standard mortar two-half-pass contact (SM2HP)

4.2.1 Finite element contact forces

In this section, an unbiased mortar formulation is obtained by applying the so-called *two-half-pass* algorithm introduced by Sauer and De Lorenzis (2013). Accordingly, the two contact surfaces are now treated equally and thus denoted by numbering (1 and 2) instead of calling them master and slave surfaces. On each contact surface, the contact pressures and the contact gaps are defined. We redefine the contact potential (20) for each contact surface separately, and consider the other surface as variationally (var.) fixed. That is,

$$\Pi_c := \int_{\Gamma_0^1} p_1^* g_n^1 dA_1 \Big|_{\Gamma^2 \text{ var. fixed}} + \int_{\Gamma_0^2} p_2^* g_n^2 dA_2 \Big|_{\Gamma^1 \text{ var. fixed}}, \quad (26)$$

where Γ^k , p_k^* , and g_n^k denote the domain, the mortar pressure (19), and the raw contact gap (7) of surface $k = 1, 2$, respectively. Taking the variation of contact potential above gives

$$\delta \Pi_c = \sum_{e \in \mathcal{E}} \delta \mathbf{x}_e \cdot \mathbf{f}_e, \quad (27)$$

where $\mathcal{E} := \mathcal{E}_s \cup \mathcal{E}_m$, and

$$\mathbf{f}_e = \int_{\Gamma_0^e} \mathbf{N}_e^T p^* \mathbf{n}_p \, dA_e . \quad (28)$$

4.2.2 Discontinuities

From Eq. (27) follows the global contact equilibrium for SM2HP

$$\sum_{A=1}^{n_1} \int_{\Gamma_0^1} N_A^1 p_1^* \mathbf{n}_p^1 \, dA_1 = \sum_{B=1}^{n_2} \int_{\Gamma_0^2} N_B^2 p_2^* \mathbf{n}_p^2 \, dA_2 , \quad (29)$$

where n_k , \mathbf{n}_p^k and N_A^k denote the number of nodes, the normal vector, and the shape functions on contact surface k , respectively. As seen, since there is no coupling term as for SMFP, the theoretical discontinuities are avoided in SM2HP. However, like for SMFP, we still must account for any *physical discontinuities* of p_k^* and/or \mathbf{n}_p^k at contact boundaries.

Note that the coupling term still appears in the tangent matrices (see Appendix A), but not in the finite element forces (28). The quadrature of the tangent matrices does not affect accuracy. Instead, it can only affect the rate of convergence for the Newton-Raphson iteration.

Therefore, segmentation is only required at the (physical) contact boundary for an accurate quadrature in SM2HP. We thus refer to this as *contact-boundary partitioning* in order to distinguish it from segmentation at overlapping boundaries of contact elements. The level-set approach presented in Duong and Sauer (2015) can be used for this purpose.

In terms of accuracy, it turns out that SM2HP is quite inaccurate. The main reason is that linear momentum balance holds only in a weak (global) sense (see Eq. (29)), while $p_1^* = p_2^*$ is not satisfied in a pointwise sense. The condition $p_1^* = p_2^*$ strongly depends on the relative discretization error between the two contact surfaces. In fact, this issue leads to the failure of the contact patch test for dissimilar meshes as will be shown later. This is in contrast to the GPTS two-half-pass approach (see Sauer and De Lorenzis (2013, 2015)) where the contact constraints are enforced pointwise.

Therefore, a further advancement of the mortar formulation is required, so that the pointwise condition $p_1^* = p_2^*$ is somehow bounded for the two-half-pass approach. At the same time, both weak and strong *physical discontinuities* at the contact boundaries still need to be treated. These issues motivate the development of the so-called *extended mortar method*, which will be presented next.

5 Extended mortar contact

This section proposes a new isogeometric mortar contact formulation based on an XFEM interpolation in order to recover the physical discontinuities of the contact pressure at contact boundaries. Therefore, the proposed contact formulation is denoted *extended mortar method*. Both its full-pass and two-half-pass version are presented.

In the following we first recapitulate the basic extended isogeometric approximation. Then this approximation is applied to the contact pressure.

5.1 Basic extended isogeometric approximation

The basic idea of extended isogeometric analysis is to enrich the original (e.g. NURBS) approximation space such that certain features like discontinuities (e.g. crack or interfaces) can be reproduced without modifying the mesh (Moës et al., 1999; De Luycker et al., 2011). This can be done by the so-called partition of unity concept. That is,

$$\sum_{A=1}^{n_s} N_A(\boldsymbol{\xi}) \psi(\boldsymbol{\xi}) = \psi(\boldsymbol{\xi}) , \quad (30)$$

where N_A are the NURBS shape functions, and ψ is an enrichment function characterizing the discontinuities of the approximated field.

We apply this approach to capture discontinuities of the mortar contact pressure (19) at contact boundaries, i.e.

$$p^* = \sum_{A=1}^{n_s} M_A \tilde{p}_A^{\text{std}} + \sum_{A=1}^{n_s} M_A \psi(\phi) \tilde{p}_A^{\text{enr}} . \quad (31)$$

Here, \tilde{p}_A^{std} and \tilde{p}_A^{enr} are nodal coefficients to be determined later, and ψ is defined by

$$\psi(\phi) := \text{sign}(\phi) = \begin{cases} 1 & \text{if } \phi > 0 , \\ 0 & \text{if } \phi = 0 , \\ -1 & \text{if } \phi < 0 , \end{cases} \quad (32)$$

where $\phi(\boldsymbol{x})$ is a level-set function defined by (Duong and Sauer, 2015)

$$\phi(\boldsymbol{x}) \begin{cases} < 0 & \text{in } \Gamma_{\text{in}}^e , \\ = 0 & \text{on } \mathcal{C}^e , \\ > 0 & \text{in } \Gamma_{\text{o}}^e . \end{cases} \quad (33)$$

Here, Γ_{in}^e and Γ_{o}^e denote in-contact and out-of-contact domains that are separated by the contact boundary \mathcal{C}^e on the contact element Γ^e . Note that the first term in Eq. (31) is the standard interpolation (19), while the second term is an enrichment term according to (30) that is included in order to reproduce a discontinuity.

Further, in order to compute the nodal coefficients \tilde{p}_A^{std} and \tilde{p}_A^{enr} , one distinguishes between extrinsic and intrinsic enrichments (see e.g. Fries and Belytschko (2006)). With extrinsic enrichment, the unknown coefficients \tilde{p}_A^{enr} associated with the enriched solution add extra degrees of freedom to the global system, while with intrinsic enrichment, \tilde{p}_A^{std} and \tilde{p}_A^{enr} are determined from a certain reproducing condition. Here, we will follow the latter approach, presented in detail in the following.

5.2 A least-squares approach

In order to determine the extra unknowns \tilde{p}_A^{enr} in Eq. (31), we consider the reproducing condition

$$g_r := p^* - \bar{p} \approx 0, \quad (34)$$

where \bar{p} is the nominal, pointwise contact pressure given by

$$\bar{p} = \epsilon_n H(\phi) g_n =: J \bar{p}^{\text{true}} . \quad (35)$$

Here, $\bar{p}^{\text{true}} = \bar{\epsilon}_n H(\phi) g_n$, and H is the Heaviside function,

$$H(\phi) = \begin{cases} 0 & \text{if } \phi \geq 0, \\ 1 & \text{if } \phi < 0. \end{cases} \quad (36)$$

To enforce condition (34), a simple method is to minimize the least-squares potential,

$$\Pi_{LS} := \int_{\Gamma_0^s} \frac{1}{2} (p^* - \bar{p})^2 dA_s. \quad (37)$$

By inserting Eq. (31) into (37) and setting $\delta\Pi_{LS} = 0$, we obtain the following system of equations

$$\begin{cases} \mathbf{n}^{\text{ss}} \tilde{\mathbf{p}}^{\text{std}} + \mathbf{n}^{\text{sx}} \tilde{\mathbf{p}}^{\text{enr}} = \boldsymbol{\lambda}, \\ \mathbf{n}^{\text{sx}} \tilde{\mathbf{p}}^{\text{std}} + \mathbf{n}^{\text{ss}} \tilde{\mathbf{p}}^{\text{enr}} = \boldsymbol{\lambda}^x, \end{cases} \quad (38)$$

where $\tilde{\mathbf{p}}^{\text{std}} := [\tilde{p}_A^{\text{std}}]$, $\tilde{\mathbf{p}}^{\text{enr}} := [\tilde{p}_A^{\text{enr}}]$,

$$\mathbf{n}^{\text{ss}} := \int_{\Gamma_0^s} \mathbf{M}_e^T \mathbf{M}_e dA_s, \quad \mathbf{n}^{\text{sx}} := \int_{\Gamma_0^s} \psi \mathbf{M}_e^T \mathbf{M}_e dA_s, \quad (39)$$

and

$$\boldsymbol{\lambda} := \int_{\Gamma_0^s} \mathbf{M}_e^T \bar{p} dA_s, \quad \boldsymbol{\lambda}^x := \int_{\Gamma_0^s} \psi \mathbf{M}_e^T \bar{p} dA_s. \quad (40)$$

By inserting Eq. (35) into Eqs. (40), we find $\boldsymbol{\lambda} = \boldsymbol{\lambda}^x$. Thus, it follows from Eq. (38) that $2\tilde{\mathbf{p}}^{\text{std}} = 2\tilde{\mathbf{p}}^{\text{enr}} =: \tilde{\mathbf{p}}$, and

$$\tilde{\mathbf{p}} = \mathbf{W}_x^{-1} \boldsymbol{\lambda}, \quad (41)$$

with

$$\mathbf{W}_x := \mathbf{n}^{\text{ss}} + \mathbf{n}^{\text{sx}} = \int_{\Gamma_0^s} H(\phi) \mathbf{M}_e^T \mathbf{M}_e dA_s. \quad (42)$$

As seen, \mathbf{W}_x is symmetric and invertible within the space spanned by the nodal active set ($\chi_A > 0$) defined by

$$[\chi_A] := H([h_A]); \quad [h_A] := - \int_{\Gamma_0^s} M_A H(\phi) dA_s. \quad (43)$$

For inactive nodes, i.e. $\chi_A = 0$, we have $\tilde{p}_A^{\text{std}} = \tilde{p}_A^{\text{enr}} = 0$.

5.3 Extended mortar contact forces

With the ingredients above, we are now able to derive an extended mortar contact formulation. For concise presentation, we assume that M_A has the same support area as N_A . Expression (31) then can be rewritten as

$$p^* = \sum_{A=1}^{n_e} M_A^x \tilde{p}_A = \mathbf{M}_x \tilde{\mathbf{p}}_e, \quad (44)$$

since $\psi(\phi) = 2H(\phi) - 1$. Here, $\mathbf{M}_x := H(\phi)\mathbf{M}_e$ denotes the extended shape function array, and $\tilde{\mathbf{p}}_e$ is the nodal pressure vector determined from Eq. (41). With expression (44), the variation of the potential (20) at the equilibrium state (i.e. $g_n \approx 0$) reads

$$\delta\Pi_c = \int_{\Gamma_0^s} p^* \delta g_n dA_s, \quad (45)$$

which has the same form as the standard case (21). Therefore, expressions (22–23) are still valid if \tilde{p}_A is computed by Eq. (41), and \mathbf{M}_e is replaced by \mathbf{M}_x . We thus obtain the so-called *extended mortar full-pass* (XMFP) as

$$\delta\Pi_c = \sum_{e \in \mathcal{E}_s} (\delta\mathbf{x}_e \cdot \mathbf{f}_e + \delta\mathbf{x}_{\hat{e}} \cdot \mathbf{f}_{\hat{e}}) , \quad (46)$$

where

$$\begin{aligned} \mathbf{f}_e &:= \int_{\Gamma_0^e} \mathbf{N}_e^T p^* \mathbf{n}_p \, dA_e = \int_{\Gamma_0^e} H(\phi) \mathbf{N}_e^T \mathbf{n}_p \mathbf{M}_e \, dA_e \tilde{\mathbf{p}}^e , \\ \mathbf{f}_{\hat{e}} &:= - \int_{\Gamma_0^e} \mathbf{N}_p^T p^* \mathbf{n}_p \, dA_e = - \int_{\Gamma_0^e} H(\phi) \mathbf{N}_p^T \mathbf{n}_p \mathbf{M}_e \, dA_e \tilde{\mathbf{p}}^e . \end{aligned} \quad (47)$$

Similar to Sec. 4.2, the *extended mortar two-half-pass* (XM2HP) reads

$$\delta\Pi_c = \sum_{e \in \mathcal{E}} \delta\mathbf{x}_e \cdot \mathbf{f}_e , \quad (48)$$

where $\mathcal{E} := \mathcal{E}_s \cup \mathcal{E}_m$ and \mathbf{f}_e are computed by Eq. (47)a.

Remark: Since the matrix \mathbf{W}_x is a global quantity, no ill-conditioning problem is to be expected when the contact boundaries approach the element boundaries. This is in contrast to standard mortar methods based on consistent dual shape functions (Popp et al., 2012).

5.4 Numerical quadrature

Since the proposed extended mortar formulation only modifies the interpolation of the contact pressure to account for physical discontinuities, the discussion of the discontinuities in Sec. 4.1.2 and 4.2.2 is still valid for XMFP and XM2HP, respectively. Thus, for XMFP, apart from the physical discontinuities appearing at the contact boundary, artificial (theoretical) discontinuities can appear at overlapping element boundaries. To treat those, either segmentation or many quadrature points is needed there. For XM2HP, discontinuities only appear at the contact boundary. In order to reduce the quadrature error associated with those, we employ RBQ (Duong and Sauer, 2015). Strictly, RBQ is only needed for strong discontinuities, e.g. at sharp corners. For weak discontinuities many quadrature points can be used instead of RBQ. But this can decrease efficiency and robustness. Since there are no discontinuities within the contact area³, a special quadrature treatment like segmentation is not needed for XM2HP.

6 A unified contact formulation

The contact virtual work for GPTS, standard mortar (21), and extended mortar (45) can be written in the combined expression

$$\delta\Pi_c = \int_{\Gamma_0^s} p^* \delta g_n \, dA_s , \quad (49)$$

with a suitable definition of the mortar contact pressure p^* . Tab. 3 summarizes the definitions of p^* for the considered contact formulations. For linearization, the interpolation for p^* in the

³In case of multiple NURBS patches, there may still be geometric discontinuities due to \mathbf{n}_p^k at patch interfaces during the deformation. This can be easily treated by applying a continuity constraint (see e.g. Duong et al. (2017a)) instead of segmentation.

Contact formulation	Contact pressure	Auxiliary parameters	Finite element forces
GPTS	$p^* := \chi p$	$p = \epsilon_n g_n$	see e.g. Wriggers (2006)
Standard mortar	$p^* := \sum_{A=1}^{n_e} M_A \tilde{p}_A$ (19)	$\tilde{\mathbf{p}} := \mathbf{A} \int_{\Gamma_0^s} \mathbf{M}_e^T p \, dA_s$	see Eq. (23)
Extended mortar	$p^* := \sum_{A=1}^{n_e} M_A^x \tilde{p}_A$ (44)	$\tilde{\mathbf{p}} := \mathbf{W}_x^{-1} \int_{\Gamma_0^s} \mathbf{M}_x^T p \, dA_s$	see Eq. (47)

Table 3: Contact pressure for various contact formulations. In the table $\mathbf{A} := \text{diag}([\chi_A])$.

mortar formulations can be further written into the unified expression

$$p^* := \sum_{A=1}^{n_e} \Phi_A \tilde{p}_A, \quad (50)$$

where Φ_A denote the unified shape functions. That is, $\Phi_A = M_A$ for standard mortar and $\Phi_A = M_A^x$ for extended mortar. The expression of the nodal parameter $\tilde{\mathbf{p}}$ can also be unified,

$$\tilde{\mathbf{p}} := \mathbf{G} \int_{\Gamma_0^s} \Phi^T p \, dA_s. \quad (51)$$

where $\mathbf{G} = \mathbf{A}$, and $\mathbf{G} = \mathbf{W}_x^{-1}$ for standard mortar and extended mortar, respectively. Details on the linearization of Eq. (49) can be found in Appendix A.

7 Contact patch test

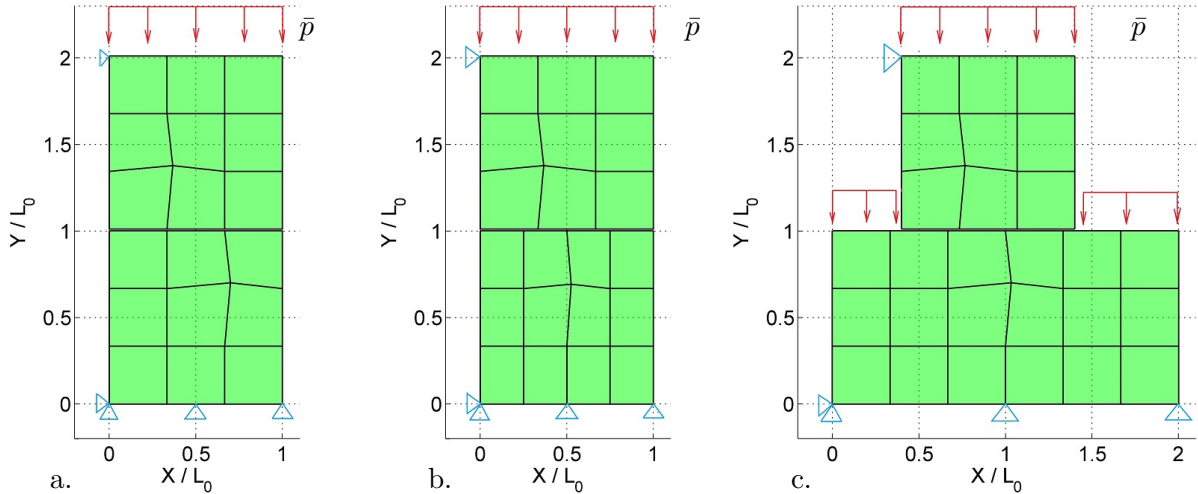


Figure 1: Contact patch tests: a. case 1: conforming mesh, b. case 2: non-conforming mesh, c. case 3: generalized patch test. \bar{p} denotes an applied uniform pressure.

This section presents a set of two-dimensional patch tests for various contact formulations. The considered formulations are GPTS full-pass (GPFP) and two-half-pass (GP2HP), standard mortar full-pass (SMFP) and two-half-pass (SM2HP), extended mortar full-pass (XMFP) and two-half-pass (XM2HP). Three test cases are examined as is shown in Fig. 1. Test case 1

(Fig. 1a), based on a conforming mesh, is used to test the ability of the contact formulations to transfer contact forces with “exact” quadrature (see Sec. 7.1). Test case 2 (Fig. 1b) is used to investigate quadrature errors due to non-conforming meshes (see Sec. 7.2). Test case 3 (Fig. 1c) is used to assess the effectiveness of RBQ in both GPTS and mortar formulations (see Sec. 7.3). Unlike in test cases 1 and 2, the RBQ technique is employed in test case 3 since there are contact elements that are partially in contact. The results are then summarized in Sec. 7.4. All simulations are based on the penalty method and frictionless contact.

7.1 Contact patch test case 1: conforming mesh

Figs. 2, 3, and 4 show the relative error in the vertical stress for GPTS, standard mortar, and extended mortar, respectively. As shown, GPTS and extended mortar (both full-pass and two-half-pass) can pass the patch test provided that penalty parameter ϵ_n is sufficiently low. This is due to the fact that in theory the error goes down to machine precision when ϵ_n increases. In practice, however, machine precision cannot be reached as the condition number of the stiffness matrix also increases, which is shown in Tab. 4. Additionally for GP2HP, according to [Sauer and De Lorenzis \(2013\)](#), large ϵ_n possibly leads to over-constraining, which prevents reaching machine precision.

The error for standard mortar, however, is high even at low ϵ_n (see Fig. 3). It improves when ϵ_n increases. The source of the error is therefore not only due to the increasing condition number, but there is also another source of error stemming from the underlying contact theory. Following the approach by [Zavarise and De Lorenzis \(2009\)](#), we further investigate the distribution of the nodal contact forces for the considered contact formulations (see Appendix B). It turns out that standard mortar in combination with the penalty method cannot reproduce a constant contact pressure exactly, which is a necessary condition to pass the patch test. Strictly speaking, for this reason the standard mortar does not pass the patch test in spite of the high accuracy shown in Fig. 3. This conclusion is in agreement with the results of [Dittmann et al. \(2014\)](#).

Test case 1 also reveals the advantage of non-partition-of-unity (non-PU) mortar shape functions (e.g. M-LmLS) over their PU counterparts (e.g. M-LmLS*). For instance, M-LmLS used for standard mortar provides less penetration and higher accuracy (see Fig. 3), yet yields the same order of condition number (see Tab. 4). These findings are also similar for all other mortar shape functions presented in Tab. 1. However, for extended mortar, there is not much difference between non-PU and PU shape functions (see Fig. 4).

7.2 Contact patch test case 2: non-conforming mesh

For non-conforming meshes, additional errors due to the mesh dissimilarity appear and affect the contact formulations. We now examine the relative error in the vertical stress considering GPTS, standard mortar and extended mortar while varying both the number of quadrature points n_{gp} and penalty parameters ϵ_n . As mentioned before, RBQ is not required in this test. Fig. 5 shows the results of SMFP and GPF. We observe that GPF passes the test within quadrature accuracy. However, both SMFP and GPF are sensitive to n_{gp} . This confirms the significance of segmentation for overlapping boundaries of master-slave elements in both formulations.

In the top row of Fig. 6, we consider SM2HP. Like SMFP, it cannot pass this patch test. A detailed investigation of the contact interface, as shown in Fig. 7a, reveals for SM2HP a significant error in the local momentum balance due to the mesh dissimilarities.

As the middle row of Fig. 6 shows, XMFP can pass the patch test within quadrature accuracy.

ϵ_n		standard mortar		extended mortar		GPTS
$[E/L]$		M-LmLS	M-LmLS*	M-LmLS	M-LmLS*	
10^0	fp	2.932e+03	4.102e+03	1.562e+03	1.562e+03	2.7276e+03
	2HP	2.587e+03	1.736e+03		1.164e+03	4.1493e+03
10^1	fp	1.462e+04	2.934e+03	2.092e+03	2.092e+03	
	2HP	7.167e+03	3.957e+03		1.863e+03	
10^2	fp	1.344e+05	1.069e+04	1.759e+04	1.759e+04	1.9307e+04
	2HP	6.773e+04	2.076e+04		1.095e+04	2.7711e+04
10^3	fp	1.333e+06	9.806e+04	1.731e+05	1.731e+05	
	2HP	6.825e+05	1.514e+05		1.046e+05	
10^4	fp	1.332e+07	9.744e+05	1.728e+06	1.728e+06	1.8103e+06
	2HP	6.832e+06	1.530e+06		1.041e+06	2.5549e+06
10^5	fp	1.332e+08	9.738e+06	1.728e+07	1.728e+07	
	2HP	6.812e+07	1.533e+07		1.041e+07	
10^6	fp	1.332e+09	9.738e+07	1.728e+08	1.728e+08	1.8091e+08
	2HP	6.812e+08	1.534e+08		1.041e+08	2.5528e+08

Table 4: Patch test for case 1 (conforming mesh): Condition number of the global stiffness matrix (accounting for contact and bulk elasticity) for increasing ϵ_n considering various contact formulations and mortar shape functions.

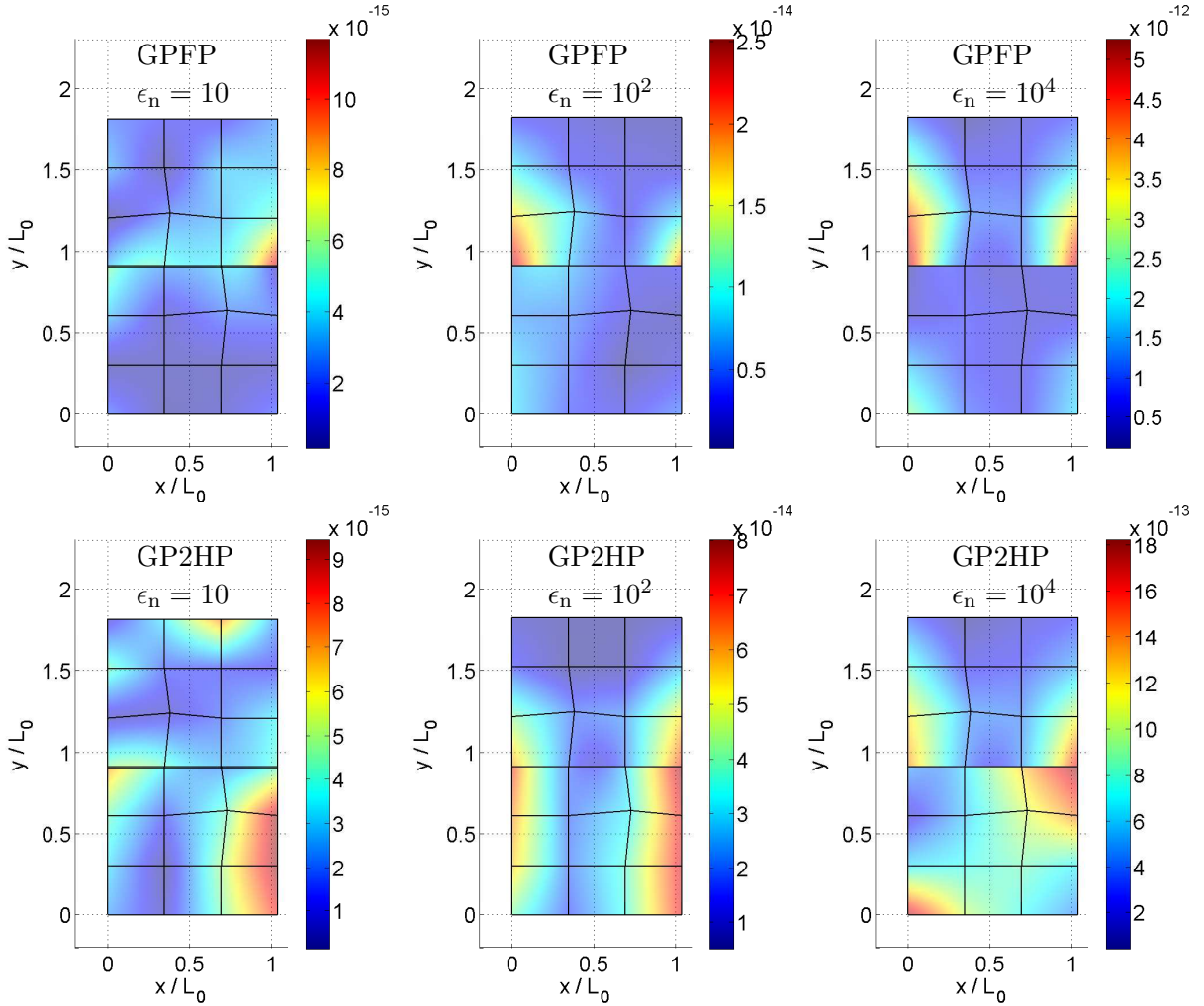


Figure 2: Patch test case 1 (conforming mesh) for **GPTS** formulations: first and second rows consider full-pass (**GFPF**) and two-half-pass (**GP2HP**) approaches, respectively, with varying penalty parameters ϵ_n . The color shows relative errors in the vertical stress.

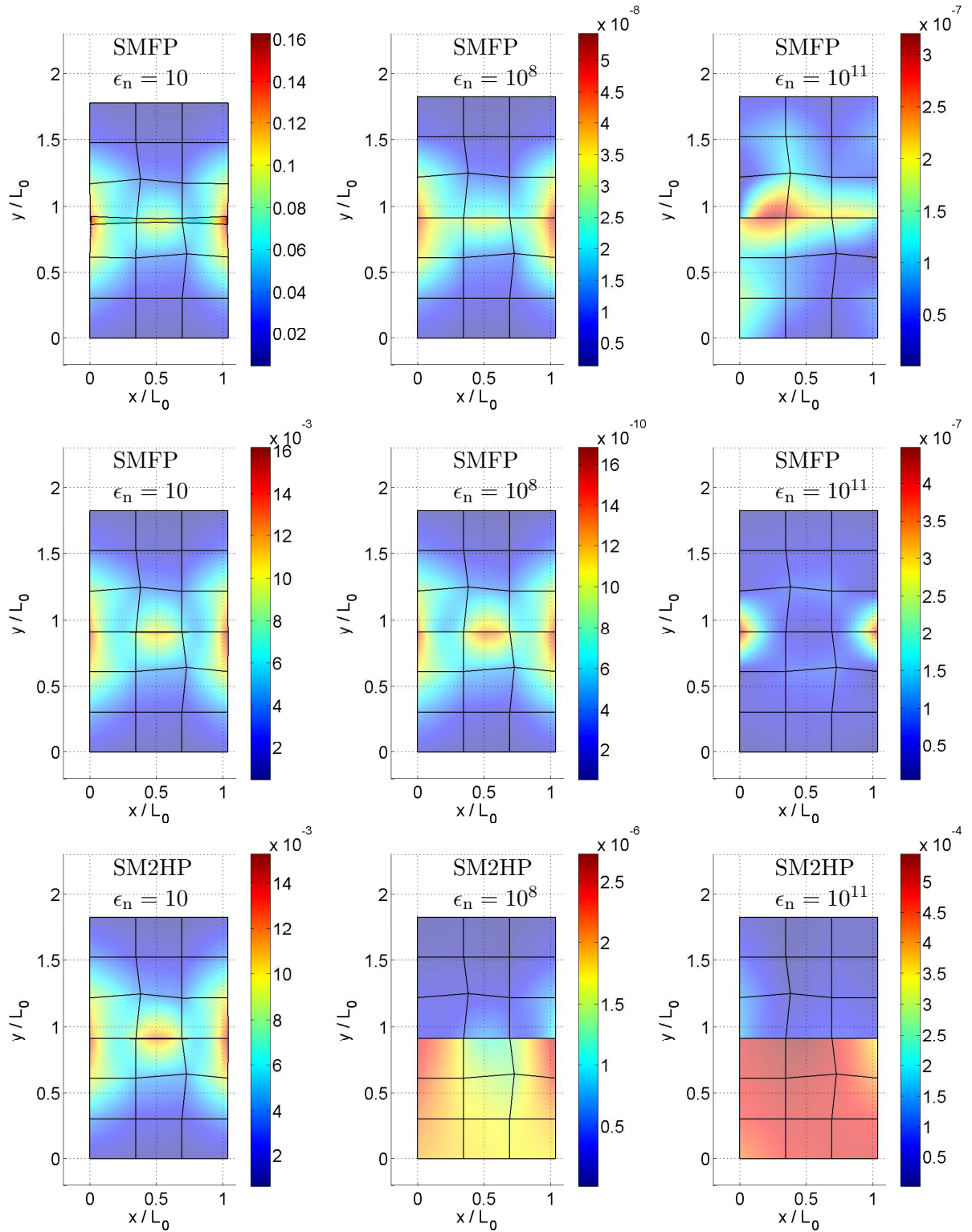


Figure 3: Patch test case 1 (conforming mesh) for **standard mortar** formulations: top and middle rows consider full-pass (**SMFP**) with shape functions M-LmLS* and M-LmLS (see Tab. 1), respectively; bottom row considers two-half-pass (**SM2HP**) with M-LmLS. Columns from left to right vary penalty parameters. The color shows relative errors in the vertical stress.

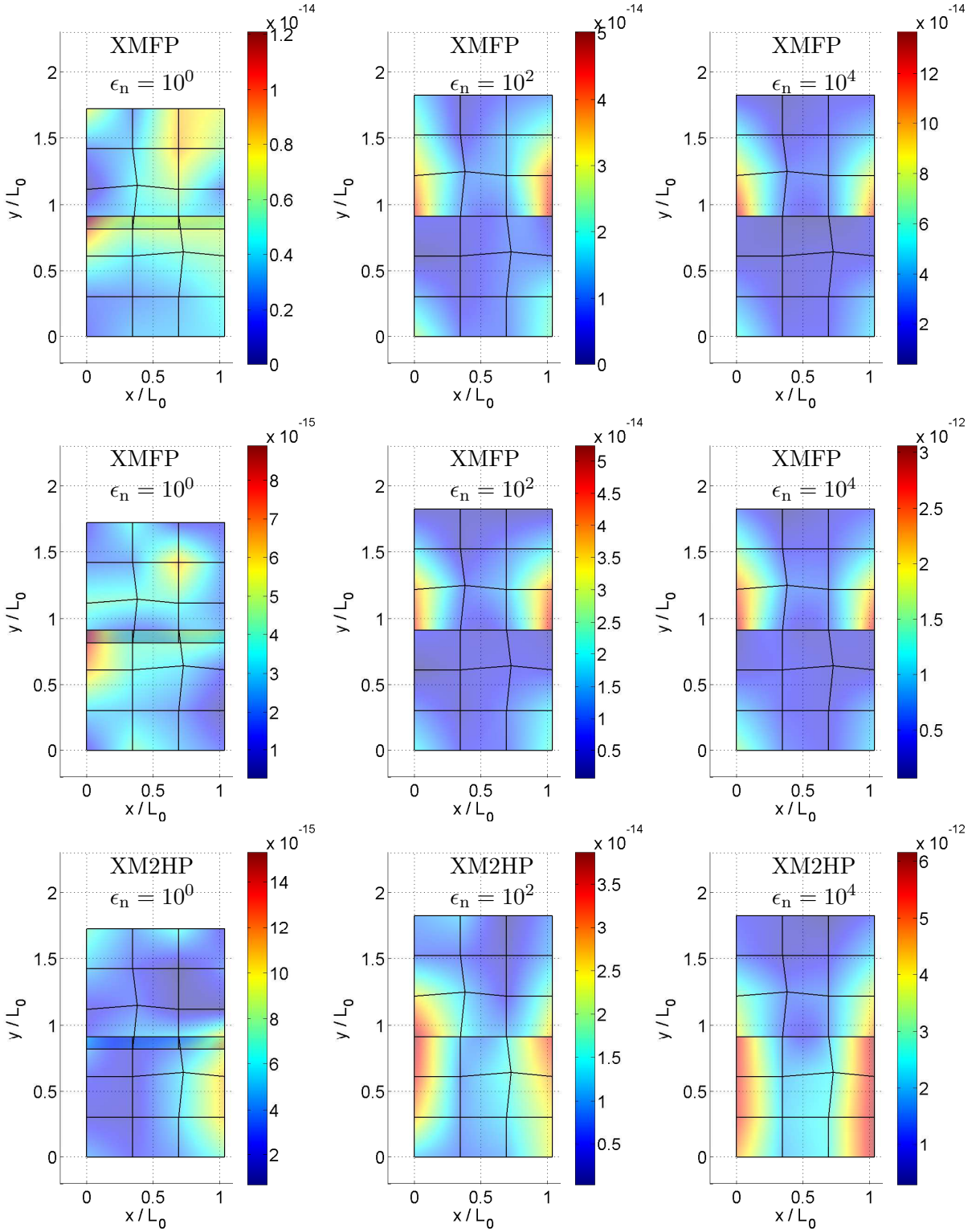


Figure 4: Patch test case 1 (conforming mesh) for **extended mortar** formulations: top and middle rows consider full-pass (**XMFP**) with shape functions M-LmLS* and M-LmLS (see Tab. 1), respectively; bottom row considers two-half-pass (**XM2HP**) with M-LmLS*. Columns from left to right vary penalty parameters. The color shows relative errors in the vertical stress.

This property is similar to the GPDF formulation (see Fig. 5). Nevertheless, this implies that the quadrature segmentation in the contact domain also plays a significant role in XMFP.

Besides, the two-half-pass version, XM2HP, can pass the test even for a small number of quadrature points (see the bottom row of Fig. 6 and Fig. 7b). Therefore, this confirms that XM2HP indeed works as a segmentation-free formulation.

7.3 Contact patch test case 3: generalized case

The last patch test examines quadrature errors at elements that are partially in contact. We focus on the influence of RBQ (Duong and Sauer, 2015) on GPDF, XMFP, and XM2HP. RBQ is distinct from segmentation (see e.g. Puso and Laursen (2004a)), since RBQ is based on an adaptive partitioning along the contact boundary on partial contact elements (Duong and Sauer, 2015). The efficiency of RBQ in comparison with segmentation thus depends on the ratio of the number of partial contact elements to the total number of contact elements. As seen in Fig. 8, without RBQ both XMFP and GPDF cannot pass the generalized patch test even when 1000 quadrature points per element are used. In contrast to this, XM2HP can reach high accuracy with only 5 Gauss points per element (both for the finite element force and tangent evaluation) without requiring any segmentation. This is shown in the bottom row of Fig. 8.

7.4 Summary of the contact patch tests

The patch test results for the considered contact formulations are summarized in Tab. 5.

Contact method	1. (conform)	2. (non-conform)	3. (generalized)
GPDF (Gauss-point-to-segment full-pass)	passed	passed*	w/o RBQ: failed w/ RBQ: passed*
GP2HP (Gauss-point-to-segment two-half-pass)	passed	passed	passed w/o RBQ
SMFP (Standard mortar full-pass)	failed	failed	failed
SM2HP (Standard mortar two-half-pass)	failed	failed	failed
XMFP (Extended mortar full-pass)	passed	passed*	w/o RBQ: failed w/ RBQ: passed*
XM2HP (Extended mortar two-half-pass)	passed	passed	passed w/o RBQ

Table 5: Summary of the three contact patch tests: Formulations GP2HP (Sauer and De Lorenzis, 2013) and XM2HP (proposed here) are the only formulations that pass all patch tests without using either segmentation or RBQ. (*) means that the patch test is only passed within quadrature accuracy.

8 Numerical examples

This section presents five examples to illustrate the robustness and accuracy of the extended mortar formulation developed in Sec. 5. We will compare extended mortar with standard mortar and classical GPTS methods. For all contact examples, quadratic NURBS will be used for the contact surfaces. In the examples, a (plane strain) Neo-Hookean material model (see e.g. Ogden (1987)) is used for (2D) 3D solids, respectively. For shells, we employ the Koiter model of Duong et al. (2017a).

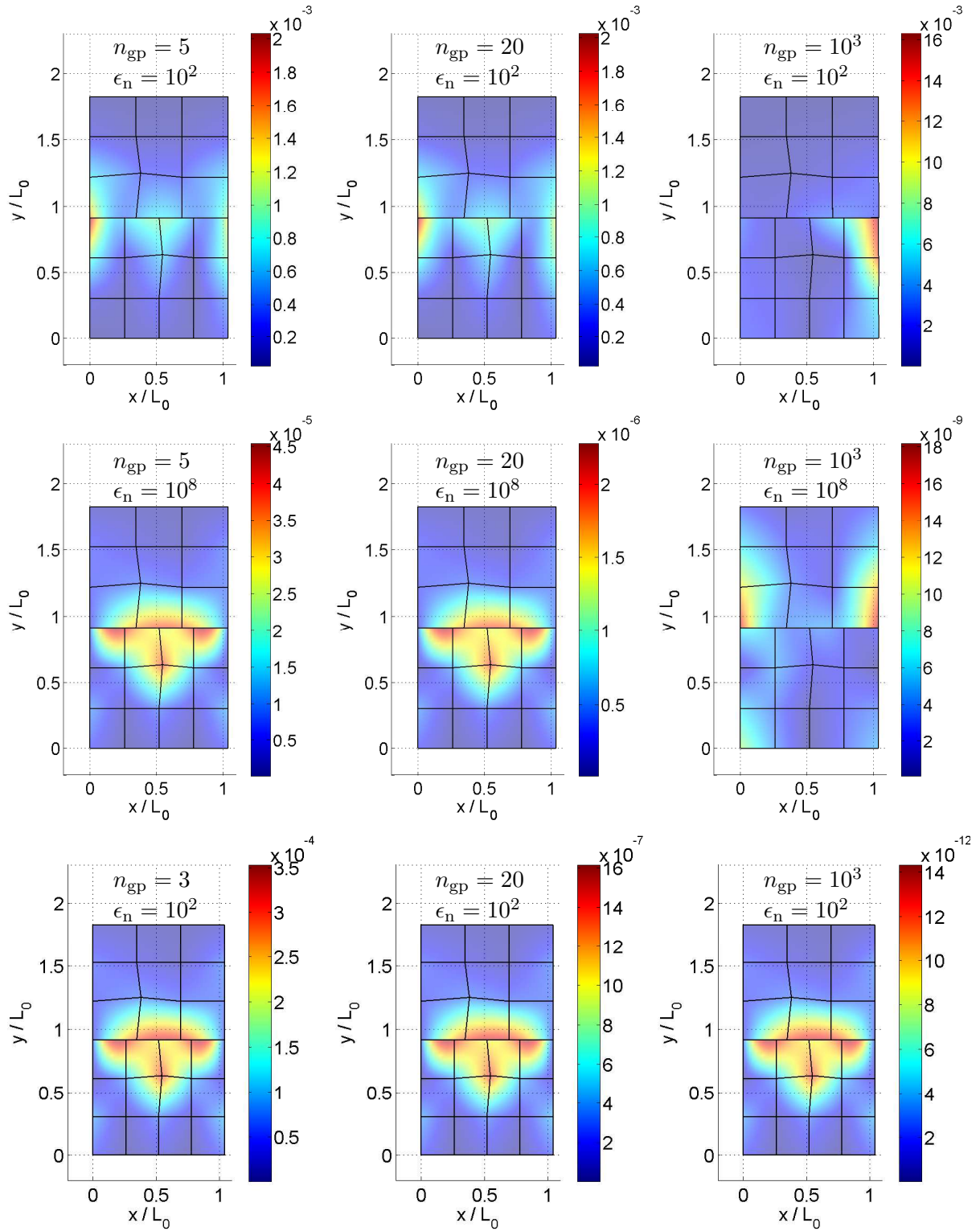


Figure 5: Patch test case 2 (non-conforming meshes): Standard mortar full-pass (**SMFP**) with mortar shape function M-LmLS (upper and middle row) versus Gauss-point-to-segment full-pass (**GFPP**) (bottom row) contact formulations varying the number of quadrature points n_{gp} and penalty parameters $\epsilon_n [E/L]$. The color shows relative errors in the vertical stress.

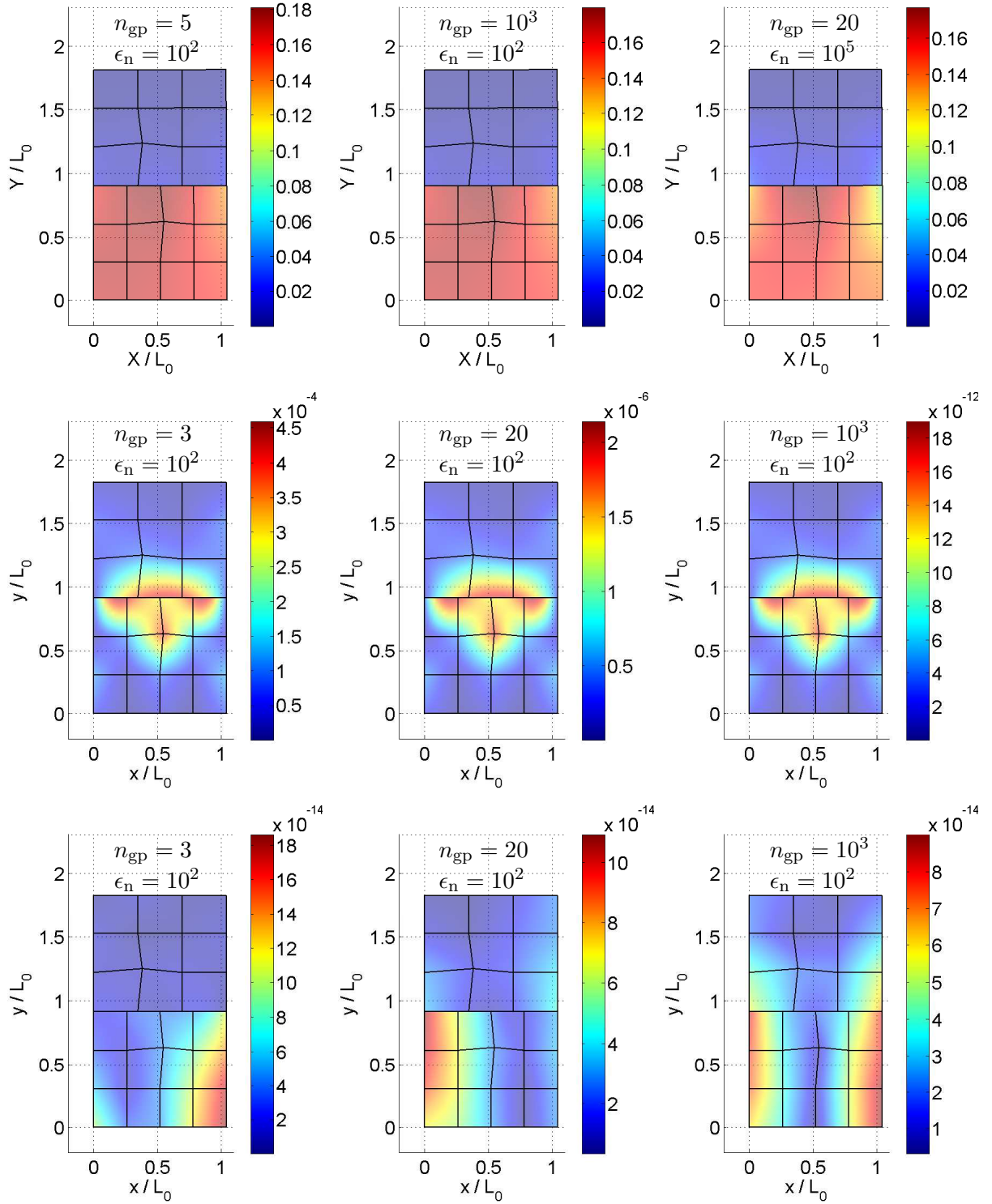


Figure 6: Patch test case 2 (non-conforming meshes): Standard mortar two-half-pass (**SM2HP**) (top row) versus extended mortar contact formulations with full-pass (**XMFP**) (middle row) and two-half-pass (**XM2HP**) (bottom row) varying n_{gp} and $\epsilon_n [E/L]$. The color shows relative errors in the vertical stress.

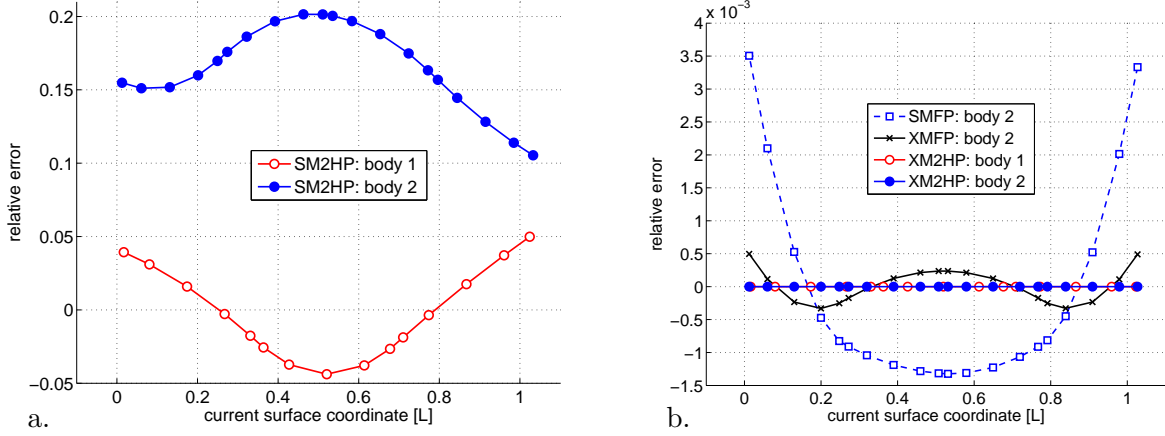


Figure 7: Patch test case 2 (non-conforming meshes) for a. standard mortar two-half-pass (SM2HP) versus b. standard mortar full-pass (SMFPP) and extended mortar two-half-pass (XM2HP): relative error of the (true) mortar contact pressure (given in Eqs. (19) and (16)) w.r.t. the exact solution along the contact interface for various mortar contact formulations. Here, $n_{gp} = 5$, $\epsilon_n = 10^2 [E/L]$ is kept fixed. For standard mortar, M-LmLS is used (see Tab. 1). The error of extended XM2HP is of the order of 10^{-12} .

8.1 2D indentation

The first example examines two-dimensional contact between a rigid cylinder and a deformable slab. The computational results are compared for three contact formulations: GPTS–RBQ, standard mortar, and extended mortar. In particular, for standard mortar, the M-LmLS and M-LcLS shape functions are used, while for extended mortar M-LmLS shape function is considered.

The initial mesh and boundary conditions are shown in Fig. 9a. Here, the bulk is discretized by linear elements, while the contact surface is enriched by quadratic NURBS elements (Corbett and Sauer, 2014). Fig. 9b shows the deformed configuration colored by the first stress invariant $I_1 = \text{tr } \boldsymbol{\sigma}$. Note that in this example, the full-pass algorithm is used. But no segmentation is required even for standard mortar, since one of the bodies is rigid and thus no master mortar shape functions are appearing in integration. However, the contact pressure has a weak physical discontinuity at the contact boundary. While this kind of discontinuity is embedded in GPTS and extended mortar, it is not accounted for in standard mortar (see Sec. 4).

The comparison of the load–displacement curve (Fig. 9c-d) shows that extended mortar provides comparable accuracy as GPTS, while standard mortar, especially with the M-LmLS shape function, gives much less accurate results (see Fig. 9c).

Fig. 10 shows the penetration at the contact interface for various contact formulations. As observed in Fig. 10c, standard mortar with M-LmLS results in an irregular penetration around the contact boundary. This implies that the weak physical discontinuity at the contact boundary induces a significant error in the standard mortar formulation with standard (M-LmLS*) or weighted standard (M-LmLS) shape functions.

In Fig. 11, we examine different measures of the contact pressure as the mesh is refined. The post-processed mortar contact pressure is obtained according to post-processing scheme of Sauer (2013). Three mesh refinement levels, $m := 2, 4$ and 8 , are plotted. Here, the exact contact pressure is obtained with a very fine mesh (mesh level $m = 128$). As seen, all the considered contact formulations converge with mesh refinement. However, in contrast to the standard mortar method, the extended mortar formulation can capture the discontinuities at the contact boundary much better with coarse meshes.

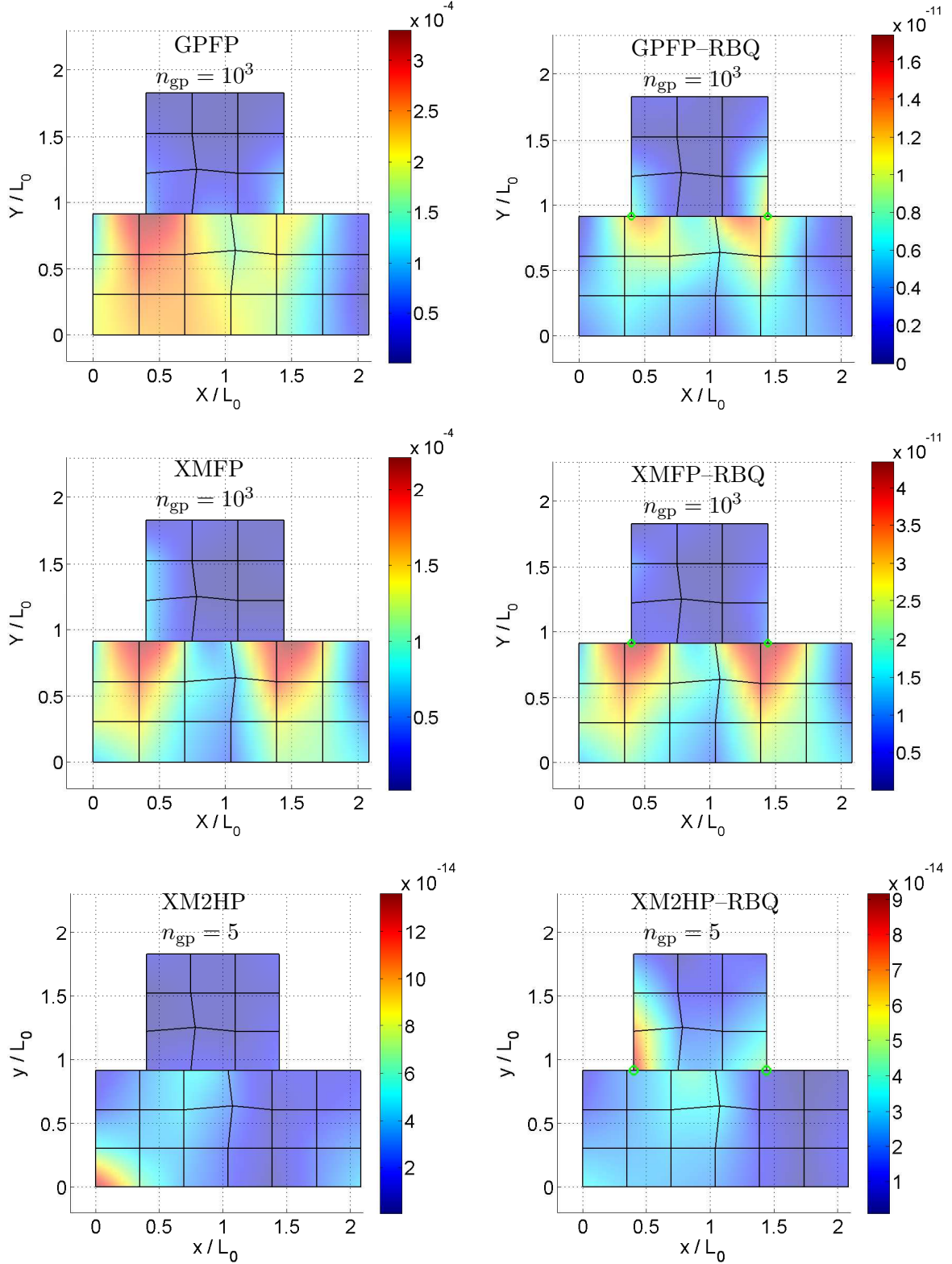


Figure 8: Patch test case 3 (generalized case): rows from top to down consider Gauss-point-to-segment full-pass (**GPF**), and extended mortar with full-pass (**XMFP**) and two-half-pass (**XM2HP**). Columns consider the quadrature without RBQ (left) and with RBQ (right). The green circles show the contact boundary of the lower block as it is obtained by the RBQ algorithm. $\epsilon_n = 10 [E/L]$. The color shows relative errors in the vertical stress.

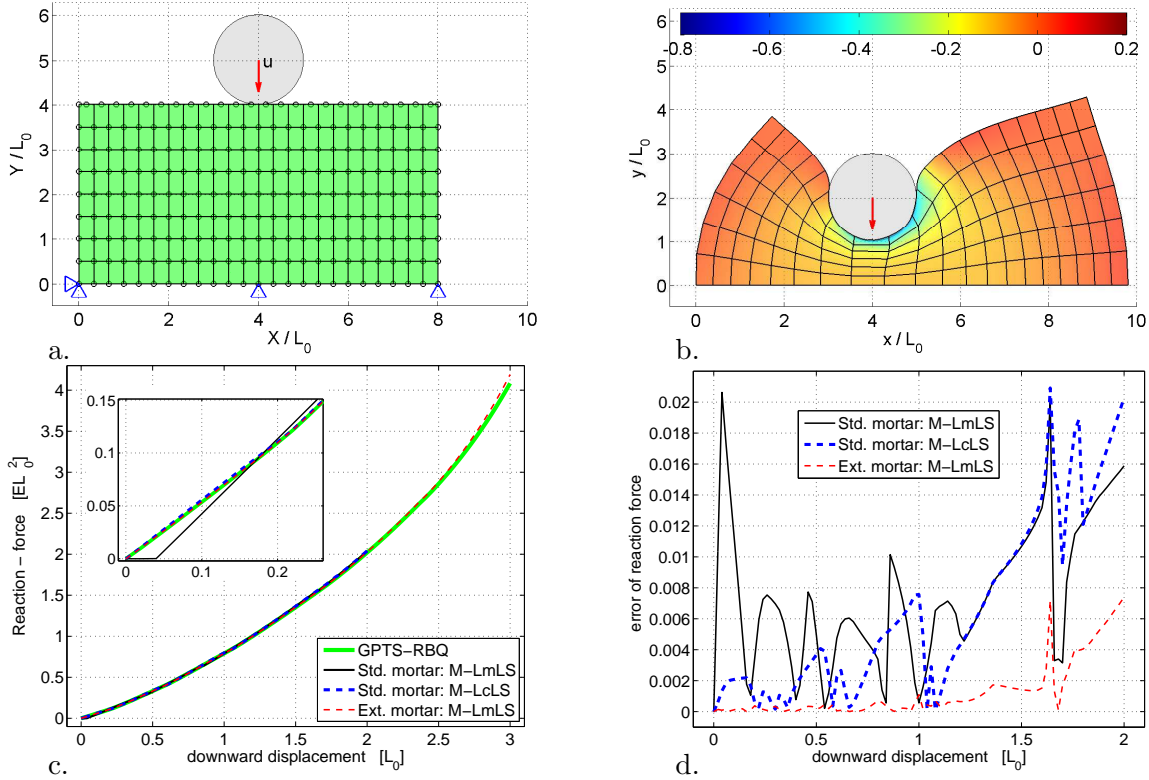


Figure 9: 2D indentation: a. Initial mesh and boundary conditions; b. Deformation computed with extended mortar for $\bar{u} = -3L_0$. c. Load–displacement curves for various contact formulations. d. Absolute error in the reaction force w.r.t the GPTS–RBQ formulation (GPTS–RBQ is used here as a reference since it is shown to be more accurate than GPTS without RBQ (Duong and Sauer, 2015)). $\epsilon_n = 100 E_0/L_0$.

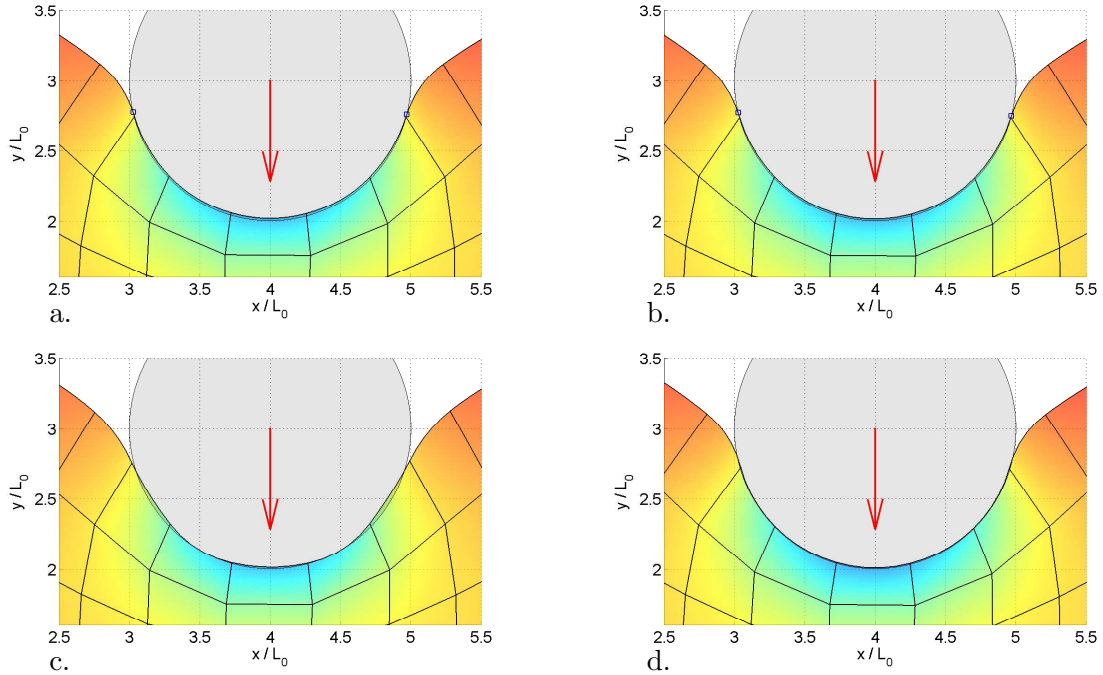


Figure 10: 2D indentation: enlargement of the contact area at $\bar{u} = -2L_0$ considering various contact formulations: a. GPTS with RBQ, b. Extended mortar with M-LmLS, c. Standard mortar with M-LmLS, and d. Standard mortar with M-LcLS.

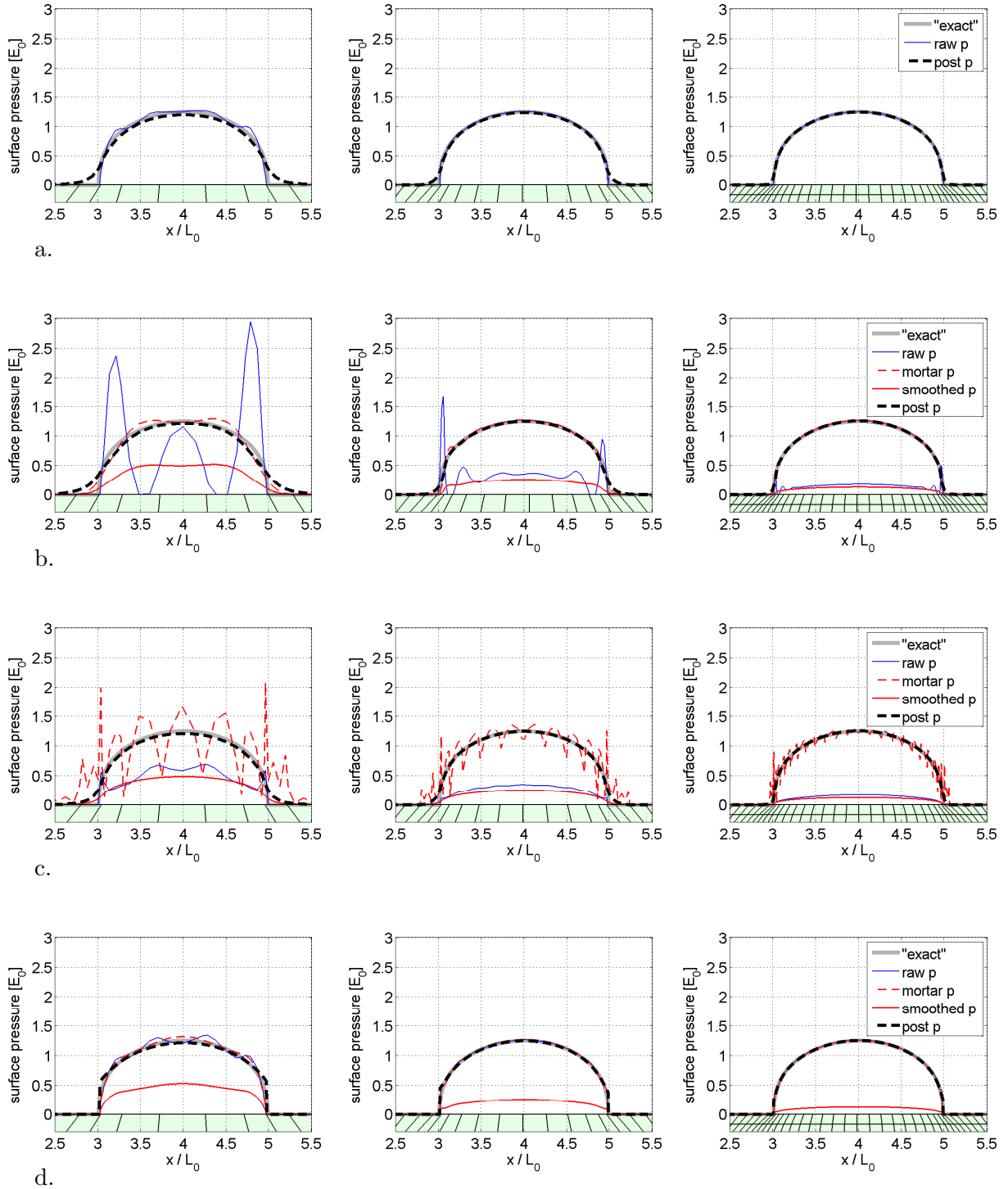


Figure 11: 2D indentation: contact pressure plotted on the flattened current surface for $\bar{u} = -2L_0$ for different mesh refinement (left to right), considering various contact formulations: a. GPTS with RBQ, b. Standard mortar with M-LmLS, c. Standard mortar with M-LcLS, and d. Extended mortar with M-LmLS.

8.2 2D ironing: circular indenter

Next, a 2D ironing problem with two deformable bodies is considered. The problem setup is shown in Fig. 12. A periodic boundary condition is applied to the left and the right sides of the slab. The bulk of the bodies is discretized by linear finite elements, while its contact surface is enriched by quadratic NURBS elements (Corbett and Sauer, 2014).

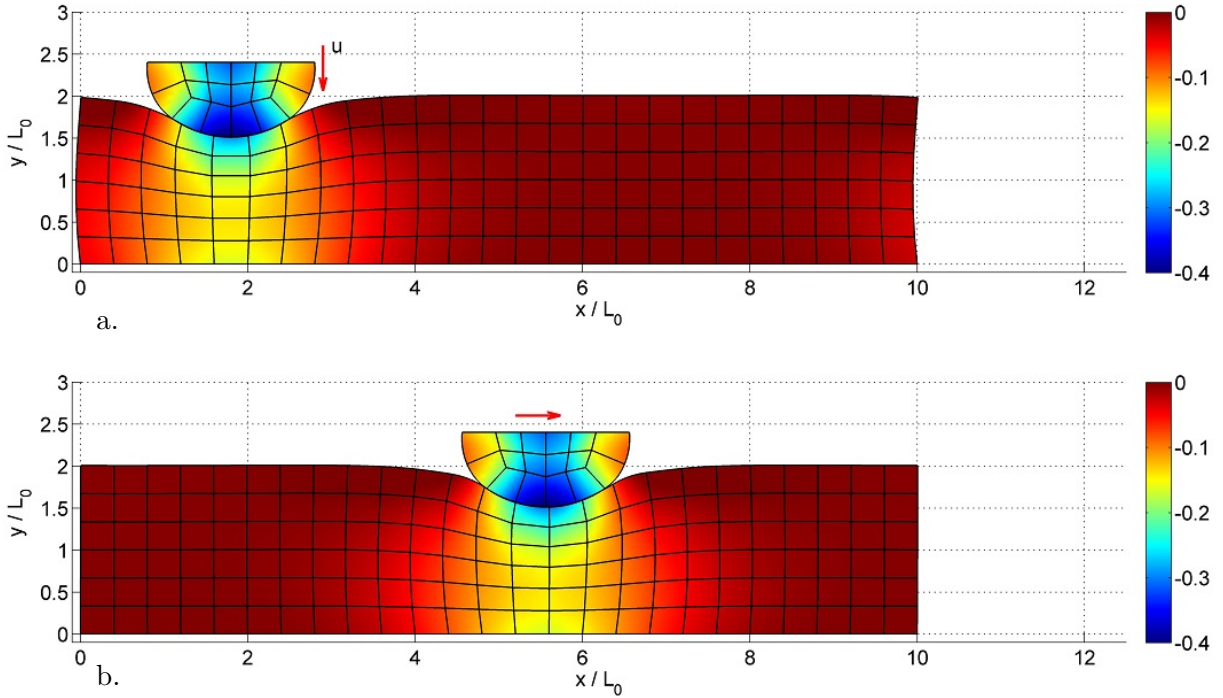


Figure 12: 2D ironing with circular indenter: a cylinder with radius $R_0 = 1$ is pressed downward until $\bar{u} = -0.6 L_0$ (a.) and then moved horizontally (b.). The color shows the first stress invariant I_1 .

This problem has been considered in Sauer and De Lorenzis (2013) for assessing the GP2HP formulation. Here, we will examine both standard mortar and extended mortar in comparison with GPTS-RBQ (considering both the full-pass and the two-half-pass approach). In the example, the shape functions M-LmLS and M-LmLS* are used for standard mortar and extended mortar, respectively. For the full-pass mortar method, we use many Gauss points ($n_{\text{gp}} = 20$) to avoid segmentation. For the two-half-pass mortar method, only 7 Gauss points are used.

In this example we observe that all the considered contact formulations can complete the simulation without any convergence problems. Plotting the load-displacement curve (see Fig. 13) reveals that SM2HP yields highly inaccurate results (Fig. 13a). XM2HP on the other hand provides an accuracy even higher than GP2HP-RBQ (Fig. 13b). Furthermore, by using RQB for GPF, the accuracy in terms of the bias error is reduced significantly as is shown in Fig. 13d. and Tab. 6. For GP2HP, RBQ also yields smoother results. In comparison with standard mortar, the accuracy of extended mortar is also improved for both the full-pass and two-half-pass approach. These results are shown in Fig. 13c-d.

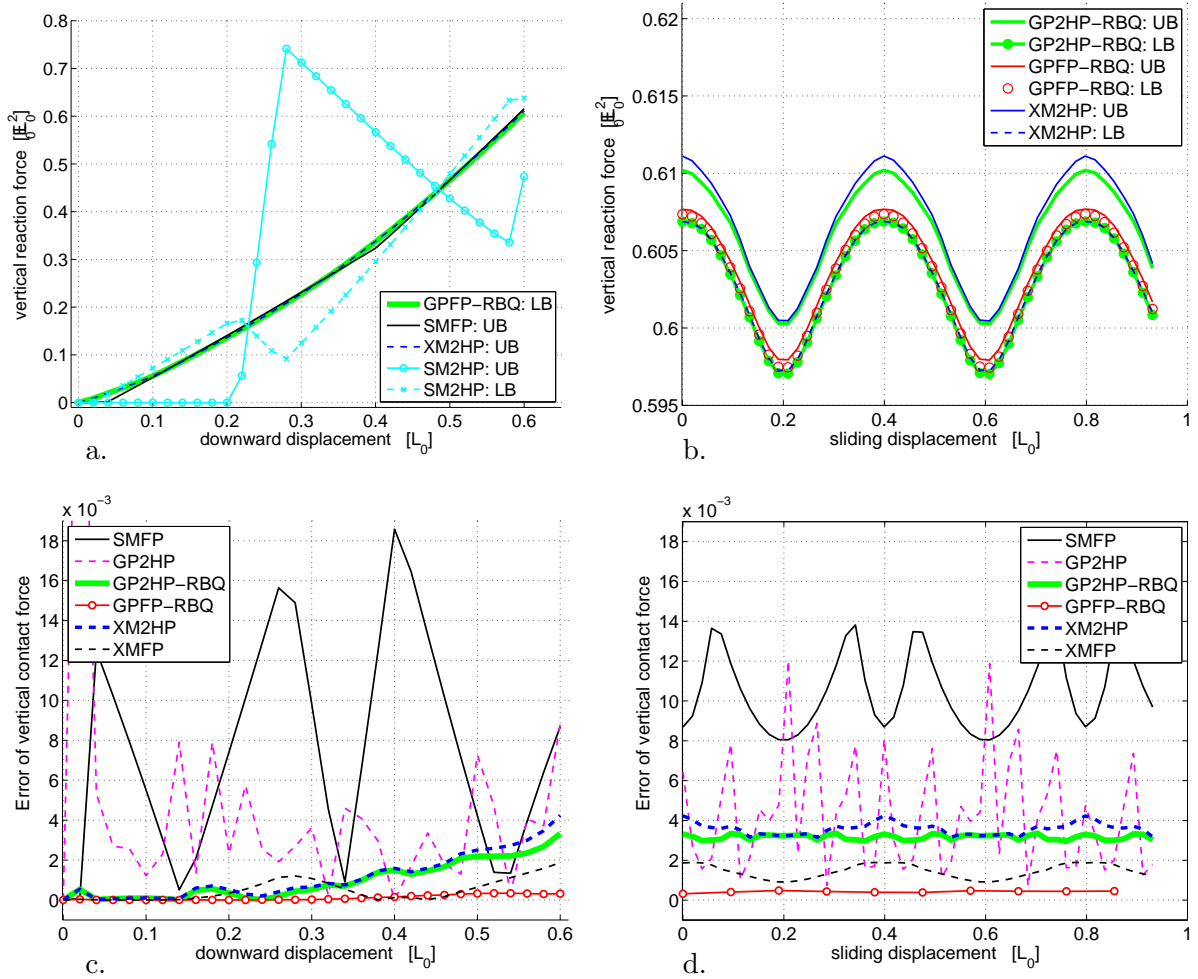


Figure 13: 2D ironing with circular indenter: Load–displacement curves for a. pressing phase and b. sliding phase; c. and d. show the bias error, defined by $|R_{UB} - R_{LB}|$, for pressing and sliding, respectively. Here, R denotes the reaction force either on the upper (UB) or lower (LB) body.

GPFP-RBQ	GP2HP	GP2HP-RBQ	SMFP	XMFP	XM2HP
4.23×10^{-04}	4.59×10^{-03}	3.18×10^{-03}	1.02×10^{-02}	1.46×10^{-03}	3.61×10^{-03}

Table 6: 2D ironing with circular indenter: the average error per sliding period obtained from Fig. 13d for each contact method.

8.3 2D ironing: square indenter

Next, we examine a square block sliding on a slab as shown in Fig. 14. The bulk of the bodies is discretized by linear finite elements, and its contact surface is enriched by quadratic NURBS elements (Corbett and Sauer, 2014). This example is challenging due to the singular contact pressure at the corners of the block. Here we also use periodic boundary conditions along the two sides of the slab. With $n_{gp} = 10$, XM2HP can complete the simulation while GPTS (both full-pass and two-half-pass) fails to converge.

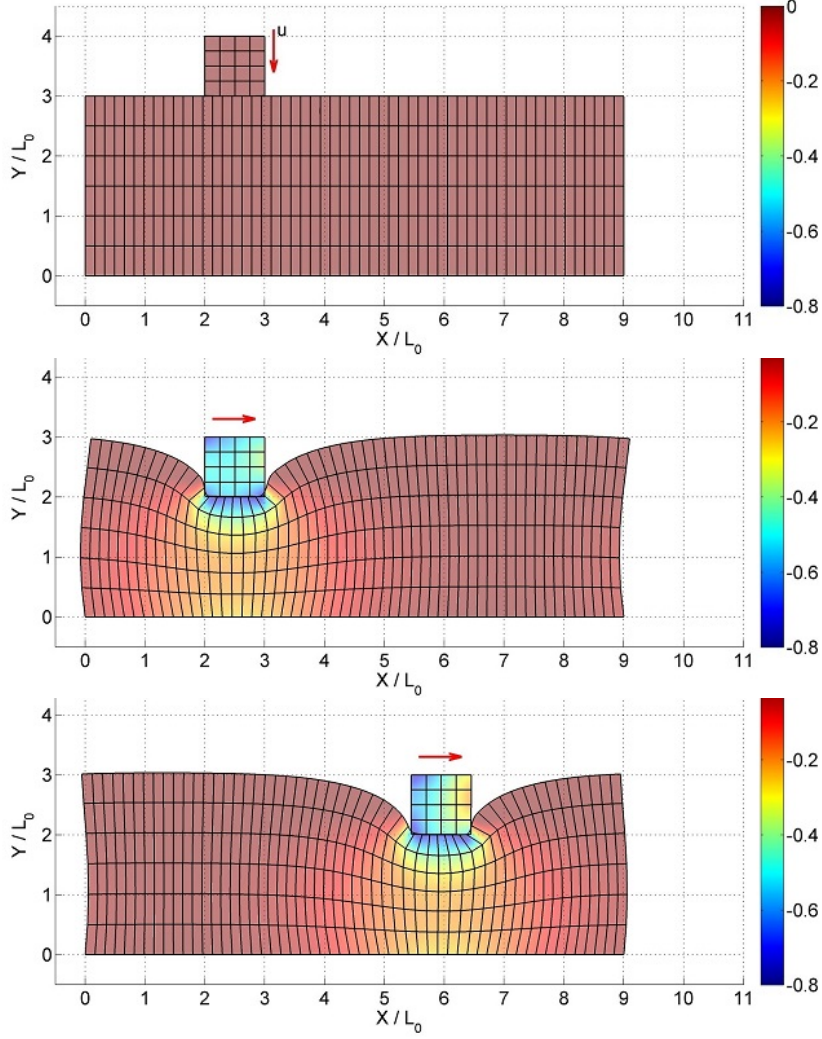


Figure 14: 2D ironing with square indenter at different snapshots of pressing and sliding. The color represents the first stress invariant I_1 . $\epsilon_n = 100 E_0/L_0$.

8.4 3D ironing

3D ironing contact between a ring and slab is considered. In this example, extended mortar (full-pass/two-half-pass) is compared with GP2HP. The setup is depicted in Fig. 15a. The geometry and the material parameters are adopted from the example presented by [Puso and Laursen \(2004a\)](#). The ring has $E = 1000 E_0$, $\nu = 0.3$, radius $R = 3 L_0$, thickness $T = 0.2 L_0$, and width $W = 5.2 L_0$, and the slab has $E = 1 E_0$, $\nu = 0.3$ and dimension $9 L_0 \times 4 L_0 \times 3 L_0$. The ring is discretized by quadratic NURBS shell elements ([Duong et al., 2017a](#)). The bulk of the slab is discretized by 3D linear finite elements, while its contact surface is enriched by quadratic NURBS elements ([Corbett and Sauer, 2014](#)).

The ring is pressed downward by $u_y = -1.4 L_0$, and then moved in X -direction. 20×20 quadrature points per element are used for the quadrature of the contact terms. The snapshots of the deformed configurations at the end of each phase are shown in Fig. 15b-c.

As seen in Fig. 15d, extended mortar gives comparable accuracy as GP2HP. Both extended mortar and GPTS can complete the simulation. For a more irregular overlapping of the meshes during sliding, we consider a twisting example in the following.

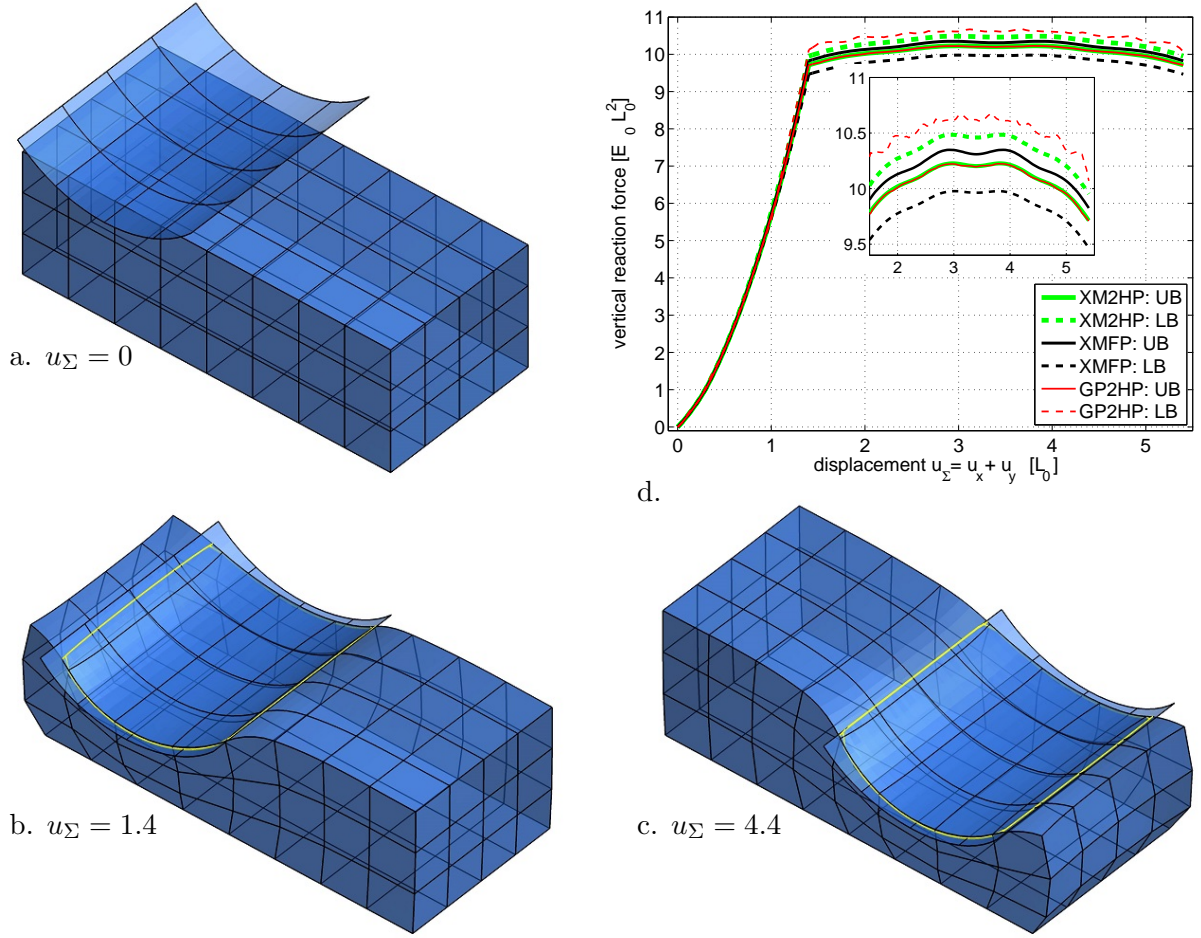


Figure 15: 3D ironing: a. initial configuration. b. and c. Deformed configurations at the end of the pressing and the sliding phase for XM2HP. Here, the yellow curve shows the detected contact boundary based on the RBQ technique (Duong and Sauer, 2015). d. Load-displacement curve for GP2HP, XMFP, and XM2HP.

8.5 Twisted blocks

In this example, the contact of two 3D blocks with dimensions $10L_0 \times 10L_0 \times 10L_0$ is simulated. The two blocks are first pressed together and then twisted against each other by prescribing $u_z = -5L_0$ and $\phi = \pi/2$, respectively, at the upper boundary of the upper block (see Figs. 16a-c). The load-displacement curves are plotted in Figs. 16d-e for extended mortar in comparison with GP2HP. In particular, both standard GP2HP and GP2HP-RBQ are examined. The penalty parameter $\epsilon = 10E_0/L_0$ and 5×5 quadrature points per element are considered in the contact simulations.

During the pressing phase, the computational results are almost identical for all considered contact formulations. This is due to the fact that no edge contact appears in this case. During the twisting phase, however, GP2HP (and GPFHP) fails to converge. For continuation, the freezing of the active-set strategy is applied here (denoted as GP2HP*), but the results tend to strongly oscillate as is seen in Fig. 16e. This is caused by the sudden contact changes at the quadrature points. In contrast to this, both GP2HP-RBQ and extended mortar (either full-pass or two-half-pass) give smooth results (see Fig. 16e). XM2HP is shown to have comparable accuracy with GP2HP-RBQ. Furthermore, in this simulation, XMFP is observed to have the least bias

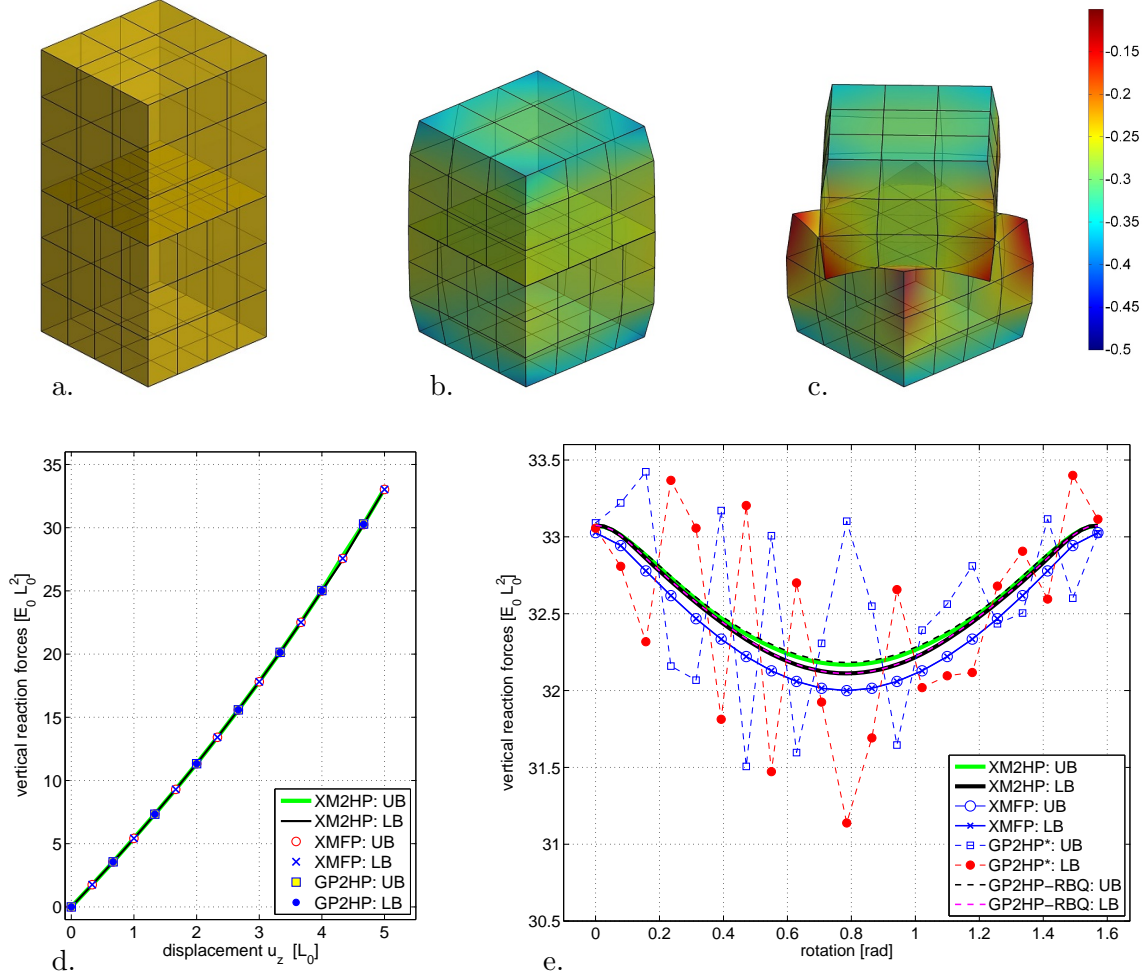


Figure 16: Twisting blocks: a. initial configuration, and deformed configurations at the end of b. the pressing phase and c. the twisting phase (at $\phi = \pi/4$). Here, the color represents the vertical stress. d-e. Load-displacement curves for various contact formulations.

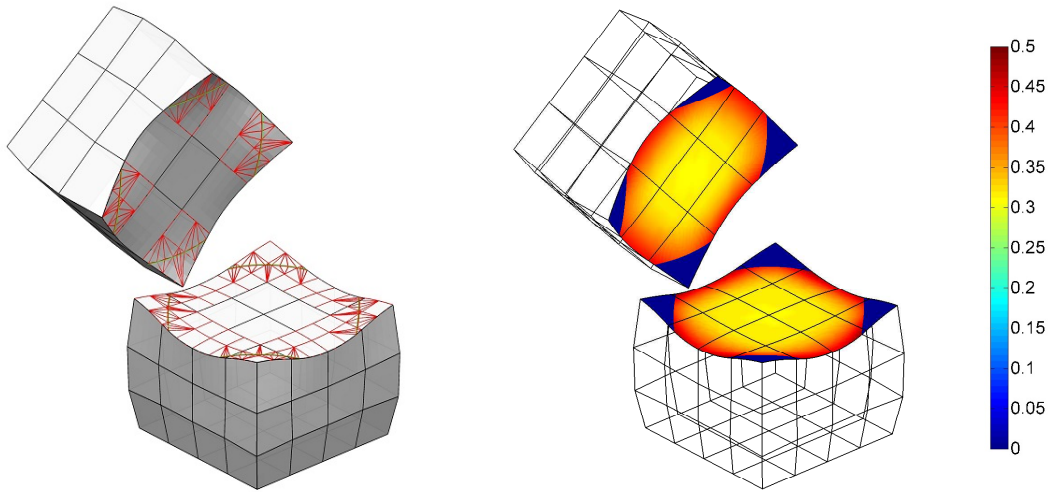


Figure 17: Twisting block: partitioning of the refined boundary quadrature (left) for the twisting phase at $\phi = \pi/4$, and post-processed contact pressure (right).

error in the vertical contact force among all considered contact formulations, even though we have not used segmentation at the overlapping element boundaries. This is seen in Fig. 16e. These results demonstrate the effectiveness of RBQ applied in the XMFP formulation.

Furthermore, Fig. 17a shows the contact boundary captured explicitly by the RBQ partitioning. With this, apart from the benefit of improving the accuracy of the interpolation and the numerical quadrature at contact boundaries, an accurate post-processing for the contact pressure can also be carried out (Duong and Sauer, 2015). This is illustrated in Fig. 17b.

9 Conclusions

A summary of the existing and proposed mortar contact formulations that have been discussed in this paper is presented in Tab. 7. In order to accurately capture *physical* discontinuities in

Items	SMFP	SM2HP	XMFP	XM2HP
Interpolation of <i>strong</i> physical discontinuities	yes	yes	yes	yes
And how?	consistency	consistency	XFEM	XFEM
Accurate quadrature of <i>strong</i> physical discontinuities	yes	yes	yes	yes
And how?	segmentation	segmentation	RBQ	RBQ
Interpolation of <i>weak</i> physical discontinuities	no	no	yes	yes
And how?	-	-	XFEM	XFEM
Accurate quadrature of <i>weak</i> physical discontinuities	no	no	yes	yes
And how?	-	-	RBQ	RBQ
Generalized contact patch test	failed	failed	passed	passed
Master/slave choice	biased	unbiased	biased	unbiased
Satisfaction of (local) momentum conservation	intrinsically	as $h \rightarrow 0$	intrinsically	as $h \rightarrow 0$

Table 7: A comparison between the standard and the extended mortar contact formulation (both with either full-pass and two-half-pass). h stands for the element size.

the contact pressure, we propose here an *extended mortar method* that is based on isogeometric analysis and XFEM enrichment. Both *weak* and *strong* physical discontinuities are captured. For the accurate quadrature at the contact boundary, the *refined boundary quadrature* (RBQ) technique (Duong and Sauer, 2015) is applied. Unlike the consistency treatment at the contact boundary of Cichosz and Bischoff (2011), extended mortar does not encounter ill-conditioning as long as the contact domain is properly refined.

Furthermore, unbiased mortar contact formulations are obtained by applying the *two-half-pass* approach (Sauer and De Lorenzis, 2013). The computational results with these formulations are independent of the choice of the slave and master surfaces. At the same time, the mortar coupling term vanishes with the two-half-pass approach. An expensive segmentation is thus not needed. The numerical examples show that SM2HP gives highly inaccurate results, while XM2HP is as robust as SMFP, and as accurate as classical GPTS.

Additionally, the contact patch test is examined for various contact formulations. It turns out that the classical mortar formulation with standard, weighted standard, and dual mortar shape functions does not pass the patch test (i.e. it cannot reach machine precision), although the accuracy in the stress is quite high (see Secs. 7.1 and 7.2). This is due to the fact that

a constant contact pressure cannot be reproduced exactly (see Appendix B). Meanwhile, the full-pass extended mortar with RBQ can pass the patch test within quadrature error. RBQ can also help GPTS full-pass to pass the patch test within quadrature error. Especially, the patch test is passed for the two-half-pass extended mortar without using segmentation and RBQ.

An important extension of this work is to the use of the Lagrange multiplier method. This would require to choose a suitable level-set function. One possible choice for this can be found in Duong and Sauer (2015). However, how this choice affects the accuracy and the efficiency should be investigated in future research. The proposed mortar method can also be extended to frictional contact following the approaches e.g. of Puso and Laursen (2004b) and Temizer et al. (2012). Another interesting extension is a consistent linearization of the RBQ procedure in order to improve the convergence of Newton iterations. In this paper, we have used an active-set strategy that avoids the linearization of the terms related to the contact boundaries. Nevertheless, it is possible to fully linearize the RBQ contributions, so that all kinds of non-linearities can be accounted for in the tangent matrices.

A Consistent linearization of contact formulations

This appendix provides a consistent linearization of various quantities for different contact formulations including classical GPTS, mortar methods, and extended isogeometric mortar method. From Eq. (49), in general we have

$$\Delta\delta\Pi_c = \sum_{e \in \mathcal{S}_s} \int_{\Gamma_0^e} (p^* \Delta\delta g_n + \Delta p^* \delta g_n) dA_e, \quad (52)$$

where $\Delta\delta g_n$ is the usual term and can be found e.g. in Sauer and De Lorenzis (2015). The term Δp^* , however, depends on the contact formulation and the choice of the mortar shape function.

A.1 Linearization of g_n

The linearization of raw gap (7) is analogous to variation (8), i.e.

$$\Delta g_n = \mathbf{n}_p \cdot (\Delta \mathbf{x} - \Delta \mathbf{x}_p), \quad (53)$$

where $\Delta \mathbf{x} = \mathbf{N}_e \Delta \mathbf{x}_e$ denotes the increment of \mathbf{x} due to a nodal increment $\Delta \mathbf{x}_e$. Note that \mathbf{x}_p depends on both \mathbf{x}_e and \mathbf{x}_e , i.e. $\mathbf{x}_p(\mathbf{x}_e, \boldsymbol{\xi}_p(\mathbf{x}, \mathbf{x}_e))$, but variation (8) and linearization (53) are still exact due to $\mathbf{n}_p \cdot \delta \mathbf{n}_p = 0$ and $\mathbf{n}_p \cdot \mathbf{a}_\alpha^p = 0$.

A.2 Linearization of δg_n

For variation (8), its linearization reads

$$\Delta\delta g_n := \Delta \mathbf{n}_p \cdot (\delta \mathbf{x} - \delta \mathbf{x}_p). \quad (54)$$

Since $\mathbf{n}_p = \mathbf{n}(\boldsymbol{\xi}_p)$ is a normalized vector and computed at projection point \mathbf{x}_p , it is a complicated function (Sauer and De Lorenzis, 2013),

$$\mathbf{n}_p = \mathbf{n}_p(\mathbf{x}, \boldsymbol{\xi}_p(\mathbf{x}, \mathbf{x}_e), g_n(\mathbf{x}, \mathbf{x}_p)). \quad (55)$$

The linearization of \mathbf{n}_p can be found in [Sauer and De Lorenzis \(2013\)](#) as

$$\Delta \mathbf{n}_p = \mathbf{P}_s \Delta \mathbf{x}_e + \mathbf{P}_m \Delta \mathbf{x}_{\hat{e}} , \quad (56)$$

where

$$\begin{aligned} \mathbf{P}_s &:= \frac{\partial \mathbf{n}_p}{\partial \mathbf{x}_e^s} = \frac{1}{g_n} (\mathbf{I} - \mathbf{n}_p \otimes \mathbf{n}_p - c_p^{\alpha\beta} \mathbf{a}_\alpha^p \otimes \mathbf{a}_\beta^p) \mathbf{N}_e , \\ \mathbf{P}_m &:= \frac{\partial \mathbf{n}_p}{\partial \mathbf{x}_{\hat{e}}} = -\frac{1}{g_n} (\mathbf{I} - \mathbf{n}_p \otimes \mathbf{n}_p - c_p^{\alpha\beta} \mathbf{a}_\alpha^p \otimes \mathbf{a}_\beta^p) \mathbf{N}_p - c_p^{\alpha\beta} \mathbf{a}_\alpha^p \otimes \mathbf{n}_p \mathbf{N}_{p,\beta} . \end{aligned} \quad (57)$$

with $c_p^{\alpha\beta} := [a_{\alpha\beta}^p - g_n b_{\alpha\beta}^p]^{-1}$. Inserting expression (56) into Eq. (54) we find

$$\begin{aligned} \Delta \delta g_n &= \delta \mathbf{x}_e \cdot (\mathbf{N}_e^T \mathbf{P}_s \Delta \mathbf{x}_e + \mathbf{N}_e^T \mathbf{P}_m \Delta \mathbf{x}_{\hat{e}}) \\ &\quad - \delta \mathbf{x}_{\hat{e}} \cdot (\mathbf{N}_p^T \mathbf{P}_s \Delta \mathbf{x}_e + \mathbf{N}_p^T \mathbf{P}_m \Delta \mathbf{x}_{\hat{e}}) . \end{aligned} \quad (58)$$

As seen, $\Delta \delta g_n$ can be computed in elementwise manner.

A.3 Linearization of p^* for GPTS

For GPTS, one has $p^* := \chi p = \chi J \bar{\epsilon}_n g_n = \chi \epsilon_n g_n$ (see Tab. 3). Since an active set strategy is used, χ is considered to be fixed. We thus have $\Delta p^* = \chi \Delta p$. Furthermore, if ϵ_n is considered fixed, the linearization of p reads

$$\Delta p = \epsilon_n \mathbf{n}_p \cdot (\Delta \mathbf{x} - \Delta \mathbf{x}_p) = \epsilon_n \mathbf{n}_p \cdot (\mathbf{N}_e \Delta \mathbf{x}_e - \mathbf{N}_p \Delta \mathbf{x}_{\hat{e}}) , \quad (59)$$

due to Eq. (53). However, if $\bar{\epsilon}_n$ is considered fixed, we need the linearization of J , which can be found in e.g. [Sauer et al. \(2014\)](#) as

$$\Delta J = J \mathbf{a}^\alpha \cdot \Delta \mathbf{a}_\alpha = \mathbf{N}_{e,\alpha} \Delta \mathbf{x}_e , \quad (60)$$

due to Eq. (2). Thus, we find

$$\Delta p = \epsilon_n \mathbf{n}_p \cdot (\mathbf{N}_e \Delta \mathbf{x}_e - \mathbf{N}_p \Delta \mathbf{x}_{\hat{e}}) + \epsilon_n \mathbf{a}^\alpha \cdot \mathbf{N}_{e,\alpha} \Delta \mathbf{x}_e , \quad (61)$$

with $\epsilon_n = J \bar{\epsilon}_n$.

A.4 Linearization of p^* and $\tilde{\mathbf{p}}$

As seen from Eq. (51), in general, the linearization of $\tilde{\mathbf{p}}$ for the mortar formulations requires the linearization of \mathbf{G} , Φ , and p . Nevertheless, in our case, \mathbf{G} and Φ are fixed since the active-set strategy is employed and the mortar shape functions M_A can be constructed such that it is independent from element distortion. Therefore, the linearization of $\tilde{\mathbf{p}}$ simplifies to

$$\Delta \tilde{\mathbf{p}} = \mathbf{G} \int_{\Gamma_0^s} \Phi_s^T \Delta p \, dA_s . \quad (62)$$

Inserting Eq. (59) into Eq. (62) for ϵ_n fixed, gives

$$\Delta \tilde{\mathbf{p}} = \mathbf{G} \int_{\Gamma_0^s} \left(\Phi_s^T \epsilon_n \mathbf{n}_p^T \mathbf{N}_e \Delta \mathbf{x}_e - \Phi_s^T \epsilon_n \mathbf{n}_p^T \mathbf{N}_p \Delta \mathbf{x}_{\hat{e}} \right) dA_s . \quad (63)$$

Here, the integral implies here the assembly into a global matrix. Thus, we can rewrite Eq. (63) into

$$\Delta \tilde{\mathbf{p}} = \mathbf{G} (\hat{\mathbf{M}}_{\text{ss}} \Delta \mathbf{x}^{\text{s}} - \hat{\mathbf{M}}_{\text{sm}} \Delta \mathbf{x}^{\text{m}}) , \quad (64)$$

where

$$\hat{\mathbf{M}}_{\text{ss}} := \int_{\Gamma_0^{\text{s}}} \boldsymbol{\Phi}_{\text{s}}^{\text{T}} \epsilon_{\text{n}} \mathbf{n}_{\text{p}}^{\text{T}} \mathbf{N}_{\text{e}} \, dA_{\text{s}} , \quad \hat{\mathbf{M}}_{\text{sm}} := \int_{\Gamma_0^{\text{s}}} \boldsymbol{\Phi}_{\text{s}}^{\text{T}} \epsilon_{\text{n}} \mathbf{n}_{\text{p}}^{\text{T}} \mathbf{N}_{\text{p}} \, dA_{\text{s}} . \quad (65)$$

Furthermore, for the linearization of p^* (see Eq. (50)), we have

$$\Delta p^* = \sum_{A=1}^{n_e} \Phi_A \Delta \tilde{p}_A = \boldsymbol{\Phi}_{\text{s}} \Delta \tilde{\mathbf{p}}^e , \quad (66)$$

since $\boldsymbol{\Phi}$ is fixed. Note that $\Delta \tilde{\mathbf{p}}^e$ is the elemental array extracted from global array $\Delta \tilde{\mathbf{p}}$.

A.5 Linearization of $\Delta \delta \Pi_{\text{c}}$: the first term

By inserting Eq. (58) into the first term of Eq. (52), we have

$$\Delta \delta \Pi_{\text{c}}^1 = \delta \mathbf{x} \cdot \mathbf{k}^1 \Delta \mathbf{x} , \quad (67)$$

where $\mathbf{x} := [\mathbf{x}^{\text{s}}; \mathbf{x}^{\text{m}}]$ contain positions of all nodes on the two contact surfaces, and \mathbf{k}^1 is defined by

$$\mathbf{k}^1 := \begin{bmatrix} \mathbf{k}_{\text{ss}}^1 & \mathbf{k}_{\text{sm}}^1 \\ \mathbf{k}_{\text{ms}}^1 & \mathbf{k}_{\text{mm}}^1 \end{bmatrix} , \quad (68)$$

and

$$\begin{aligned} \mathbf{k}_{\text{ss}}^1 &:= \int_{\Gamma_0^{\text{s}}} \mathbf{N}_{\text{e}}^{\text{T}} p^* \mathbf{P}_{\text{s}} \, dA_{\text{s}} , & \mathbf{k}_{\text{sm}}^1 &:= \int_{\Gamma_0^{\text{s}}} \mathbf{N}_{\text{e}}^{\text{T}} p^* \mathbf{P}_{\text{m}} \, dA_{\text{s}} , \\ \mathbf{k}_{\text{ms}}^1 &:= \int_{\Gamma_0^{\text{s}}} \mathbf{N}_{\text{p}}^{\text{T}} p^* \mathbf{P}_{\text{s}} \, dA_{\text{s}} , & \mathbf{k}_{\text{mm}}^1 &:= \int_{\Gamma_0^{\text{s}}} \mathbf{N}_{\text{p}}^{\text{T}} p^* \mathbf{P}_{\text{m}} \, dA_{\text{s}} . \end{aligned} \quad (69)$$

A.6 Linearization of $\Delta \delta \Pi_{\text{c}}$: the second term

For the second term in Eq. (52), we consider GPTS and mortar formulation separately.

A.6.1 For GPTS

Inserting Eqs. (8) and (59) (considering ϵ_{n} fixed) into the second term of Eq. (52), leads to

$$\Delta \delta \Pi_{\text{c}}^2 = \delta \mathbf{x} \cdot \mathbf{k}^2 \Delta \mathbf{x} , \quad (70)$$

where \mathbf{k}^2 is the tangent matrix associated with the second term of Eq. (52), given by

$$\mathbf{k}^2 := (\chi \epsilon_{\text{n}}) \begin{bmatrix} \mathbf{k}_{\text{ss}}^2 & \mathbf{k}_{\text{sm}}^2 \\ \mathbf{k}_{\text{ms}}^2 & \mathbf{k}_{\text{mm}}^2 \end{bmatrix} , \quad (71)$$

with

$$\begin{aligned} \mathbf{k}_{\text{ss}}^2 &:= \int_{\Gamma_0^{\text{s}}} \mathbf{N}_{\text{e}}^{\text{T}} \mathbf{n}_{\text{p}} \otimes \mathbf{n}_{\text{p}} \mathbf{N}_{\text{e}} \, dA_{\text{s}} , & \mathbf{k}_{\text{sm}}^2 &:= \int_{\Gamma_0^{\text{s}}} \mathbf{N}_{\text{e}}^{\text{T}} \mathbf{n}_{\text{p}} \otimes \mathbf{n}_{\text{p}} \mathbf{N}_{\text{p}} \, dA_{\text{s}} , \\ \mathbf{k}_{\text{ms}}^2 &:= \int_{\Gamma_0^{\text{s}}} \mathbf{N}_{\text{p}}^{\text{T}} \mathbf{n}_{\text{p}} \otimes \mathbf{n}_{\text{p}} \mathbf{N}_{\text{e}} \, dA_{\text{s}} , & \mathbf{k}_{\text{mm}}^2 &:= \int_{\Gamma_0^{\text{s}}} \mathbf{N}_{\text{p}}^{\text{T}} \mathbf{n}_{\text{p}} \otimes \mathbf{n}_{\text{p}} \mathbf{N}_{\text{p}} \, dA_{\text{s}} . \end{aligned} \quad (72)$$

A.6.2 For mortar formulations

Inserting Eqs. (8) and (66) into the second term of Eq. (52), gives

$$\Delta\delta\Pi_c^2 = \left(\delta\mathbf{x}^s \cdot \int_{\Gamma_0^s} \mathbf{N}_e^T \mathbf{n}_p \Phi_s dA_s - \delta\mathbf{x}^m \cdot \int_{\Gamma_0^s} \mathbf{N}_p^T \mathbf{n}_p \Phi_s dA_s \right) \Delta\tilde{\mathbf{p}} \quad (73)$$

The integrals here imply the assembly into a global matrix. Thus, we can rewrite this expression as

$$\Delta\delta\Pi_c^2 = \left(\delta\mathbf{x}^s \cdot \mathbf{M}_{ss}^T - \delta\mathbf{x}^m \cdot \mathbf{M}_{sm}^T \right) \Delta\tilde{\mathbf{p}}, \quad (74)$$

where

$$\mathbf{M}_{ss} := \int_{\Gamma_0^s} \Phi_s^T \epsilon_n \mathbf{n}_p^T \mathbf{N} dA_s, \quad \mathbf{M}_{sm} := \int_{\Gamma_0^s} \Phi_s^T \epsilon_n \mathbf{n}_p^T \mathbf{N}_p dA_s. \quad (75)$$

Furthermore, by inserting Eq. (64) into Eq. (74), we finally get the same form as Eq. (70), where \mathbf{k}^2 is now given by

$$\mathbf{k}^2 := \begin{bmatrix} \mathbf{k}_{ss}^2 & \mathbf{k}_{sm}^2 \\ \mathbf{k}_{ms}^2 & \mathbf{k}_{mm}^2 \end{bmatrix}, \quad (76)$$

and

$$\begin{aligned} \mathbf{k}_{ss}^2 &:= \mathbf{M}_{ss}^T \mathbf{G} \hat{\mathbf{M}}_{ss}, & \mathbf{k}_{sm}^2 &:= -\mathbf{M}_{ss}^T \mathbf{G} \hat{\mathbf{M}}_{sm}, \\ \mathbf{k}_{ms}^2 &:= -\mathbf{M}_{sm}^T \mathbf{G} \hat{\mathbf{M}}_{ss}, & \mathbf{k}_{mm}^2 &:= \mathbf{M}_{sm}^T \mathbf{G} \hat{\mathbf{M}}_{sm}. \end{aligned} \quad (77)$$

Here \mathbf{M}_{ss} , \mathbf{M}_{sm} , $\hat{\mathbf{M}}_{ss}$, $\hat{\mathbf{M}}_{sm}$, and \mathbf{G} are all global matrices.

A.6.3 For two-half-pass algorithm

For two-half-pass algorithm, since the master surface is considered to be variationally fixed, all associated stiffness matrices, i.e. \mathbf{k}_{mm} and \mathbf{k}_{ms} , in Eqs. (68), (71), (76) are disregarded.

B Distribution of nodal contact forces

This appendix examines the ability to reproduce a constant contact pressure in the simple patch test for various contact formulations with penalty regularization (see Fig. 18). This is in fact a necessary condition for passing the patch test of a contact formulation (Zavarise and De Lorenzis, 2009).

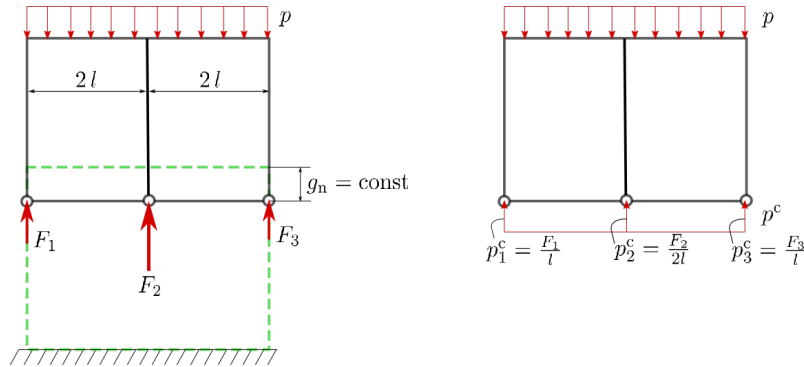


Figure 18: The simple patch test: (left) nodal contact forces F_i and (right) the equivalent distributed contact pressure p^c for two linear finite elements. A necessary condition to pass the patch test is $p_1^c = p_2^c = p_3^c$.

Fig. 18 (left) shows the contact patch test of two contact bodies with constant penetration g_n . Consider the upper (slave) body discretized by two linear elements. We denote F_i ($i = 1, 2, 3$) as the concentrated nodal forces at the three nodes on the contact surface, respectively. These concentrated nodal forces are equivalent to the distributed contact pressure p^c , which can be evaluated discretely at the nodes by (see Fig. 18 (right))

$$p_i^c = \frac{F_i}{l_i^c} \quad (\text{no sum}), \quad (78)$$

where l_i^c denote the tributary areas, which are equal to l , $2l$, and l for $i = 1, 2, 3$, respectively. To pass the patch test, we must have a constant distribution of the contact pressure, i.e. $p_1^c = p_2^c = p_3^c$. Equivalently, the normalized concentrated nodal forces \bar{F}_i should be $[1, 2, 1]^T$. In the following we will check this condition for the NTS, GPTS, standard mortar, and extended mortar formulations.

The classical NTS contact: The contact constraint is enforced directly at nodes. For the penalty method, this leads to $[\bar{F}_1, \bar{F}_2, \bar{F}_3]^T = [1, 1, 1]$. With this, since $p_1^c = p_3^c \neq p_2^c$, NTS cannot pass the patch test (also see e.g. Zavarise and De Lorenzis (2009)).

The classical GPTS contact: The magnitude of the nodal contact forces can be computed as (see e.g. Sauer and De Lorenzis (2013))

$$[F_1, F_2, F_3]^T = \int_{\Gamma} \mathbf{N}_e^T t \, dA = [tl, 2tl, tl]^T, \quad (79)$$

where the linear shape functions have been applied. We thus have $[\bar{F}_1, \bar{F}_2, \bar{F}_3]^T = [1, 2, 1]$, i.e. $p_1^c = p_2^c = p_3^c = t$, which confirms that classical GPTS can pass the patch test.

The standard mortar contact: For the sake of simplicity, we demonstrate the computation of the nodal contact forces for $\mathbf{M}_e = \mathbf{N}_e$ (i.e. M-LmLS*). Results for other mortar shape functions are listed in Tab. 8.

The weighted nodal pressures follows from Eq. (17) as

$$[\tilde{p}_1, \tilde{p}_2, \tilde{p}_3]^T = \int_{\Gamma} \mathbf{N}_e^T t \, dA = [tl, 2tl, tl]^T. \quad (80)$$

With this, the magnitude of the nodal contact forces can be computed as (see Eq. (23))

$$\begin{bmatrix} F_1 \\ F_2 \\ F_3 \end{bmatrix} = \int_{\Gamma} \mathbf{N}_e^T \mathbf{N}_e \, dA \begin{bmatrix} \tilde{p}_1 \\ \tilde{p}_2 \\ \tilde{p}_3 \end{bmatrix} = \frac{l}{3} \begin{bmatrix} 2 & 1 & 0 \\ 1 & 4 & 1 \\ 0 & 1 & 2 \end{bmatrix} \begin{bmatrix} \tilde{p}_1 \\ \tilde{p}_2 \\ \tilde{p}_3 \end{bmatrix} = \frac{tl^2}{3} \begin{bmatrix} 4 \\ 10 \\ 4 \end{bmatrix}. \quad (81)$$

Therefore, for standard mortar, we have $[\bar{F}_1, \bar{F}_2, \bar{F}_3]^T = [1, 5/2, 1]$. So it turns out that standard mortar methods cannot pass the patch test. This explains the computational results in Secs. 7.1 and 7.2. As shown in Tab. 8 with other mortar shape functions, standard mortar methods cannot pass the patch test either. It is important to note, that the ability to reproduce a constant mortar pressure p^* , not necessarily a constant smoothed pressure \hat{p} , is crucial to pass the patch test. All considered shape functions in the standard mortar method fail to do so.

M-GLS	M-GLS*	M-LmLS	M-LmLS*	M-LcLS	M-LcLS*
[1, 1, 1]	[1, 4, 1]	[1, 8/5, 1]	[1, 5/2, 1]	[1, 1, 1]	[1, 4, 1]

Table 8: Normalised concentrated nodal contact forces considering various mortar shape functions.

The extended mortar contact: In this case, the weighted nodal pressures are computed from Eq. (41) as

$$\begin{bmatrix} \tilde{p}_1 \\ \tilde{p}_2 \\ \tilde{p}_3 \end{bmatrix} = \left[\int_{\Gamma} \mathbf{M}_e^T \mathbf{M}_e \, dA \right]^{-1} \int_{\Gamma} \mathbf{M}_e^T t \, dA, \quad (82)$$

where \mathbf{M} can be any mortar shape function (see Tab. 1). With this, the magnitude of the nodal contact forces reads (see Eq. (47))

$$\begin{bmatrix} F_1 \\ F_2 \\ F_3 \end{bmatrix} = \int_{\Gamma} \mathbf{N}_e^T \mathbf{M}_e \, dA \begin{bmatrix} \tilde{p}_1 \\ \tilde{p}_2 \\ \tilde{p}_3 \end{bmatrix} = \int_{\Gamma} \mathbf{N}_e^T t \, dA, \quad (83)$$

which is identical to Eq. (79). Therefore, extended mortar can pass the patch test.

Acknowledgements

The authors are grateful to the German Research Foundation (DFG) for supporting this research under grants GSC 111 and SA1822/8-1.

References

- Brivadis, E., Buffa, A., Wohlmuth, B., and Wunderlich, L. (2015). Isogeometric mortar methods. *Comput. Methods Appl. Mech. Engrg.*, **284**(Supplement C):292 – 319.
- Cichosz, T. and Bischoff, M. (2011). Consistent treatment of boundaries with mortar contact formulations using dual Lagrange multipliers. *Comput. Methods Appl. Mech. Engrg.*, **200**:1317–1332.
- Corbett, C. J. and Sauer, R. A. (2014). NURBS-enriched contact finite elements. *Comput. Methods Appl. Mech. Engrg.*, **275**:55–75.
- De Lorenzis, L., Wriggers, P., and Hughes, T. J. R. (2014). Isogeometric contact: A review. *GAMM Mitteilungen*, **37**:85–123.
- De Lorenzis, L., Wriggers, P., and Zavarise, G. (2012). A mortar formulation for 3D large deformation contact using NURBS-based isogeometric analysis and the augmented Lagrangian method. *Comput. Mech.*, **49**:1–20.
- De Luycker, E., Benson, D. J., Belytschko, T., Bazilevs, Y., and Hsu, M. C. (2011). X-fem in isogeometric analysis for linear fracture mechanics. *Int. J. Numer. Meth. Engrg.*, **87**:541–565.
- Dittmann, M., Franke, M., Temizer, I., and Hesch, C. (2014). Isogeometric analysis and thermomechanical mortar contact problems. *Comp. Meth. Appl. Mech. Engrg.*, **274**:192–212.
- Duong, T. X., Roohbakhshan, F., and Sauer, R. A. (2017a). A new rotation-free isogeometric thin shell formulation and a corresponding continuity constraint for patch boundaries. *Comput. Methods Appl. Mech. Engrg.*, **316**:13–28.
- Duong, T. X. and Sauer, R. A. (2015). An accurate quadrature technique for the contact boundary in 3D finite element computations. *Comput. Mech.*, **55**(1):145–166.

- Duong, X. T., Lorenzis, L. D., and Sauer, R. A. (2017b). On the shape functions for the contact pressure in mortar methods. In von Scheven, M., Keip, M.-A., and Karajan, N., editors, *Proceedings of the 7th GACM Colloquium on Computational Mechanics*, pages 130–133.
- Fries, T.-P. and Belytschko, T. (2006). The intrinsic XFEM: a method for arbitrary discontinuities without additional unknowns. *Int. J. Numer. Meth. Engrg.*, **68**:1358–1385.
- Hartmann, S. and Ramm, E. (2008). A mortar based contact formulation for non-linear dynamics using dual Lagrange multipliers. *Finite Elem. Anal. Des.*, **44**:245–258.
- Hesch, C. and Betsch, P. (2008). A mortar method for energy-momentum conserving schemes in frictionless dynamic contact problems. *Int. J. Numer. Meth. Engrg.*, **77**:1468–1500.
- Hesch, C. and Betsch, P. (2011). Transient three-dimensional contact problems: Mortar method. Mixed methods and conserving integration. *Comput. Mech.*, **48**:461–475.
- Hughes, T. J. R., Cottrell, J. A., and Bazilevs, Y. (2005). Isogeometric analysis: CAD, finite elements, NURBS, exact geometry and mesh refinement. *Comp. Meth. Appl. Mech. Engrg.*, **194**:4135–4195.
- Kim, J.-Y. and Youn, S.-K. (2012). Isogeometric contact analysis using mortar method. *Int. J. Numer. Meth. Engrg.*, **89**(12):1559–1581.
- Moës, N., Dolbow, J., and Belytschko, T. (1999). A finite element method for crack growth without remeshing. *Int. J. Numer. Meth. Engrg.*, **46**:131–150.
- Ogden, R. W. (1987). *Non-Linear Elastic Deformations*. Dover Edition, Mineola.
- Popp, A., A. Seitz, M. G., and Wall, W. (2013). Improved robustness and consistency of 3D contact algorithms based on a dual mortar approach. *Comput. Methods Appl. Mech. Engrg.*, **264**:67–80.
- Popp, A., Wohlmuth, B. I., Gee, M. W., and Wall, W. A. (2012). Dual quadratic mortar finite element methods for 3D finite deformation contact. *SIAM J. Sci. Comput.*, pages B421–B446.
- Puso, M. A. and Laursen, T. A. (2004a). A mortar segment-to-segment contact method for large deformation solid mechanics. *Comput. Methods Appl. Mech. Engrg.*, **193**:601–629.
- Puso, M. A. and Laursen, T. A. (2004b). A mortar segment-to-segment frictional contact method for large deformations. *Comput. Methods Appl. Mech. Engrg.*, **193**:4891–4913.
- Sauer, R. A. (2013). Local finite element enrichment strategies for 2D contact computations and a corresponding postprocessing scheme. *Comput. Mech.*, **52**(2):301–319.
- Sauer, R. A. and De Lorenzis, L. (2013). A computational contact formulation based on surface potentials. *Comput. Methods Appl. Mech. Engrg.*, **253**:369–395.
- Sauer, R. A. and De Lorenzis, L. (2015). An unbiased computational contact formulation for 3D friction. *Int. J. Numer. Meth. Engrg.*, **101**:251–280.
- Sauer, R. A., Duong, T. X., and Corbett, C. J. (2014). A computational formulation for constrained solid and liquid membranes considering isogeometric finite elements. *Comput. Methods Appl. Mech. Engrg.*, **271**:48–68.
- Seitz, A., Farah, P., Kremheller, J., Wohlmuth, B. I., Wall, W. A., and Popp, A. (2016). Isogeometric dual mortar methods for computational contact mechanics. *Comput. Methods Appl. Mech. Engrg.*, **301**:259–280.

- Temizer, I. (2012). A mixed formulation of mortar-based frictionless contact. *Comput. Methods Appl. Mech. Engrg.*, **223-224**:173–185.
- Temizer, I., Wriggers, P., and Hughes, T. (2011). Contact treatment in isogeometric analysis with NURBS. *Comput. Methods Appl. Mech. Engrg.*, **200**:1100–1112.
- Temizer, I., Wriggers, P., and Hughes, T. J. R. (2012). Three-dimensional mortar-based frictional contact treatment in isogeometric analysis with NURBS. *Comput. Methods Appl. Mech. Engrg.*, **209-212**:115–128.
- Wilking, C. and Bischoff, M. (2017). Alternative integration algorithms for three-dimensional mortar contact. *Comput. Mech.*, **59**:203–218.
- Wriggers, P. (2006). *Computational Contact Mechanics*. Springer, 2nd edition.
- Zavarise, G. and De Lorenzis, L. (2009). A modified node-to-segment algorithm passing the contact patch test. *Int. J. Numer. Meth. Engrg.*, **79**:379–416.